Distinct hypothalamus-habenula circuits govern risk preference

Dominik Groos[1,2†], Anna Maria Reuss[2,3,5], Peter Rupprecht[1,5], Tevye Stachniak[1], Shuting Han[1], Christopher Lewis[1], Yaroslav Sych[1,4], Martin Wieckhorst[1], Theofanis Karayannis[1,2], Adriano Aguzzi[2,3], Fritjof Helmchen[1,2†]

[1]Brain Research Institute, University of Zurich, Winterthurerstrasse 190, 8057 Zurich, Switzerland

[2]Neuroscience Center Zürich, University of Zurich

Winterthurerstrasse 190, 8057 Zurich, Switzerland

[3]Institute of Neuropathology, University Hospital Zürich

Schmelzbergstrasse 12, 8091 Zurich, Switzerland

[4]Present address: Institute of Cellular and Ìntegrative Neuroscience 8 All. Du General Rouvillois, 67000, Strasbourg, France

[5]These authors contributed equally: Anna Maria Reuss, Peter Rupprecht

Number of main text pages: 9

Number of main figures: 4

Total number of words: 3732

Abstract: 213 words

Number of references: 54

†Correspondence:

Dominik Groos; Fritjof Helmchen

E-mail: groos@hifo.uzh.ch; helmchen@hifo.uzh.ch; Phone: +41 44 635 33 40

Keywords: Lateral habenula, risky decision-making, risk preference, hypothalamus

Abstract

Appropriate evaluation of risk is essential for survival in complex, uncertain environments. Confronted with choosing between a certain (safe) and an uncertain (risky) option, animals of various species show strong preferential traits which are stable across extended periods of time[1-8]. How such risk preference is encoded in the neural circuitry of the brain remains poorly understood. A candidate brain region is the lateral habenula (LHb), which has been shown to be prominently involved in various value-guided behaviors[9-12]. Here, using a balanced two-alternative choice task involving risk of loss, we find that neuronal activity in the LHb prior to action selection reflects risk preference and is governed by distinct inputs from hypothalamic subregions. Specifically, by employing multi-fiber photometry and targeted optogenetic perturbations, we identified glutamatergic LHb projections from both lateral and medial hypothalamus (LH/MH) that provide functionally distinct synaptic inputs to the LHb before action selection. Microendoscopic two-photon calcium imaging revealed risk-preference-selective LHb neurons that decreased their selectivity upon chemogenetic silencing of MH but not LH inputs. Finally, optogenetic stimulation of MH→LHb axons evoked both excitatory and inhibitory postsynaptic responses in LHb neurons (indicative of glutamate/GABA co-release for fine-tuned gain control[13]), whereas LH→LHb projections were purely excitatory. Our results thus reveal functionally distinct hypothalamus-habenula circuits that govern risk preference in situations of economic decision-making.

Main Text

The ability to choose the most favorable among multiple alternatives is key for an animal's survival and reproduction in a complex, uncertain environment. When an agent confronts multiple alternatives, it calculates costs and benefits and assigns value-based preferences to all available options. These processes are known to involve neuromodulatory regions in the mid- and

hindbrain[14-18]. A main regulator of these regions, via strong excitatory projections, is the evolutionary conserved lateral habenula (LHb), which in turn receives glutamatergic and GABAergic long-range inputs from various regions in the forebrain, thereby functionally connecting the fore- with mid- and hindbrain[19-23]. Whereas the LHb is mainly known for encoding negative motivational value[10] and aversion[11,12], as well as for its pathological transformation in major depressive disorder[24-27], it also has been implicated in the evaluation of economic risk. Specifically, pharmacological inactivation of the LHb in rats annihilated the ability to make economically favourable decisions when presented with a choice between different probabilistic reward outcomes[9]. However, how LHb circuits engage in risky decision-making remains an open question.

To address this question, we trained head-fixed mice in a balanced two-alternative choice task. Performing this task, mice could choose between two waterspouts delivering various amounts of reward upon licking. The ‘safe’ spout delivered a reward of 5 µl sucrose water in 100% of cases whereas the ‘risky’ spout delivered either 17 µl in 25% or 1 µl in 75% of all cases (Fig. 1a). Hence, the mean expected value was equal for both options. In every session, mice performed 50 forced-choice trials where in each trial only one spout (indicated by a light-emitting diode, LED) delivered a reward upon licking (with size according to safe or risky side), followed by 300 free-choice trials where both spouts carried a potential reward. Facing these two alternative options, most animals displayed a strong preference for either the safe or the risky option whereas only a few animals frequently switched between spouts (Fig. 1b, c; Methods). In the following, we refer to these different types of individuals as ‘risk-averse’ (n = 26), ‘risk-prone’ (n = 15), and ‘risk-neutral’ mice (n = 4). Mice maintained their risk preference level (defined as the likelihood of choosing its preferred option; Methods) throughout the balanced reward sessions, although control experiments showed that mice did still evaluate the available options, as they adapted their

choices whenever the expected value of one option became advantageous over the other (Extended Data Fig. 1a).

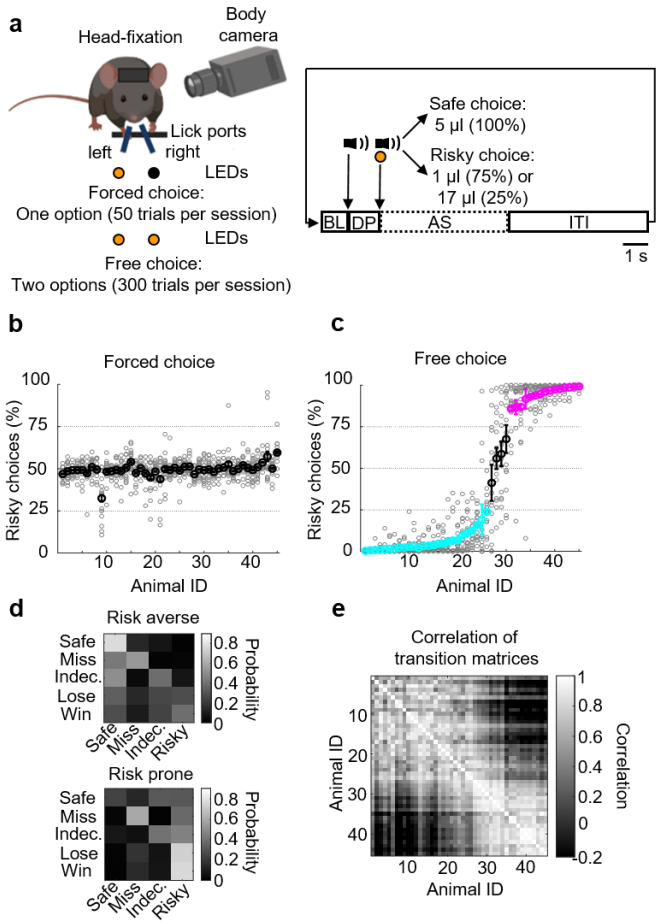

Fig. 1 | Mice display strong preferential traits for safe or risky options that are stable across time. **a**, Task structure of two-alternative choice task. After a 1-s baseline period (BL) an auditory tone indicates the start of the deliberation period (DP), which terminates with the reward-indicating cues (auditory tone paired with illumination of one or two LEDs), and is followed by the action selection (AS) and the inter-trial interval (ITI) period. **b,** Fraction of risky choices during forced choice trials (n = 45 mice). Each light grey circle represents the fraction of risky choices in an individual session (n = 14 sessions for each mouse). Dark circles are mean ± s.e.m. **c**, Same as b but for the free choice trials. Based on their choice preference mice were classified as risk-averse (cyan), risk-prone (magenta), or risk-neutral (black). **d**, Averaged transition matrices for risk-averse (top) and risk-prone (bottom) mice. Y-axis indicates previous trial outcome (Safe, Miss, Indecisive (Indec.), Lose, or Win) and X-axis the choice in the current trial. Grey values represent transition probabilities. **e**, Correlation of individual transition matrices across mice.

Risk-averse and risk-prone animals further differed in their strategies coping with loss. Whereas risk-averse individuals were more likely to switch to the safe option or show 'indecisive' behaviour (see Methods) after a loss, risk-prone animals would rather engage in a risky choice again or skip a trial (Fig. 1d; Extended Data Fig. 1b,c). Consequently, a correlation matrix of behavioural

transitions clearly segregated risk-averse vs. risk-prone individuals into risk preference-based clusters (Fig. 1e). This divergence of risk-preference across individuals might partially be explained by different levels of motivation (Extended Data Fig. 1d) but we observed no differences in either decision confidence (defined as the fraction of decisive trials; Extended Data Fig. 1e; Methods) nor in anxiety levels as assessed by the elevated plus-maze test (Extended Data Fig. 1f-h).

Based on the finding that pharmacological LHb inhibition prevents the formation of choice preferences in animals freely choosing between two probabilistic options[9] (even if one option is unambiguously advantageous over the alternative), we aimed to record LHb activity during the two-alternative choice task. To monitor neuronal activity in the LHb, we expressed Cre-dependent GCaMP6f in the LHb of Vglut2-Cre mice (n = 9) and applied fiber photometry (Fig. 2a,b). Surprisingly, we found that the glutamatergic LHb population calcium signal was consistently larger for the individuals' preferred option (be it safe or risky) prior to action selection, i.e., in the deliberation period between start and reward cue (Fig. 1a; Fig. 2c,d). This effect was abolished when we sorted fluorescence traces based on the previous choice (Fig. 2e), indicating that LHb signaling in the deliberation period reflects information related to upcoming choices rather than encoding past outcomes[5]. LHb population activity in the reward period (1-s window after valve opening) or the post-reward period (1 to 5 s after valve opening) were not able to explain risk-taking behaviour of individuals to a similar extent (Extended Data Fig. 2). Furthermore, the difference in LHb activity during the deliberation period for preferred vs. non-preferred choices could not be explained by elevated motor actions (Extended Data Fig. 3). In addition, we recorded extracellular action potentials in the LHb and found that multi-unit activity in the deliberation period was higher for preferred choices, confirming that our photometry results represent increased neuronal spiking activity in the LHb (Extended Data Fig. 4).

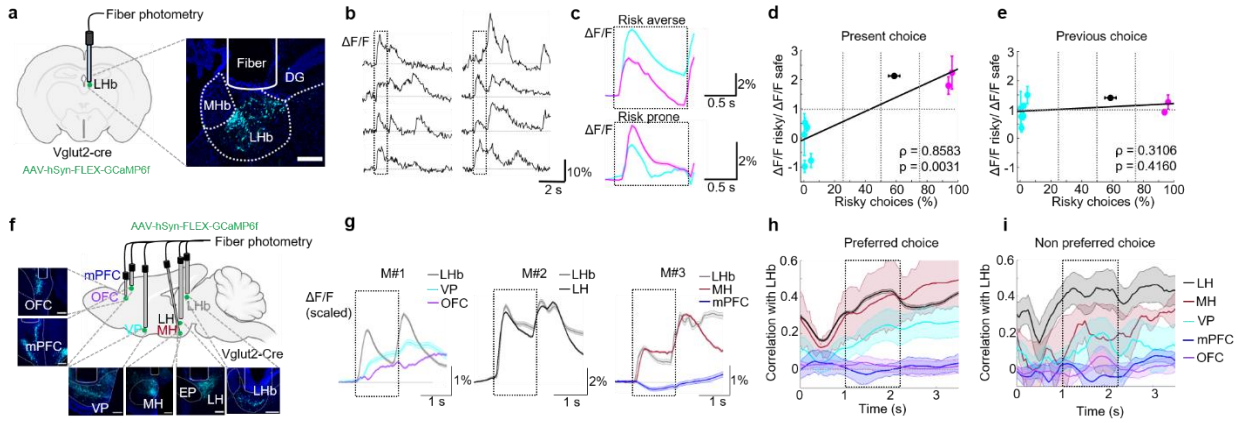

Fig. 2 | LHb population activity reflects risk preference and correlates with distinct glutamatergic inputs. a, Left: Illustration of fiber-photometric recordings in the LHb. Right: Confocal image of GCaMP6f-expressing LHb neurons with the fiber position indicated. Medial habenula (MHb), dentate gyrus (DG). Scale bar 200 µm. **b**, Examples of single-trial fiber-photometric calcium traces. Dashed boxes indicate deliberation period. **c**, LHb population activity during the deliberation period prior to safe (cyan) and risky (magenta) choices, exemplified for a risk-averse mouse (top, 2917 safe and 62 risky choice trials) and a risk-prone mouse (bottom 103 safe and 1510 risky choice trials). Data are plotted as mean ± 95% c.i. **d** and **e**, Ratio of the ΔF/F integrals during the deliberation period for risky and safe choice population activity for the present (d) and the previous (e) trial, respectively, plotted against fraction of risky choices (n = 9 mice). Data are plotted as mean ± s.e.m. **f**, Illustration of multi-fiber photometry recordings. Entopeduncular nucleus (EP). **g**, Example traces of all preferred choice trials from three animals. Data are plotted as mean ± s.e.m. **h** and **i**, Single-trial correlations of population activity in LHb input regions with LHb activity for preferred (h) and non-preferred (i) choices (averaged across trials). Dashed box, deliberation period. Data are plotted as mean ± s.e.m. Correlations from the same regions are merged across animals (n = 2-6 mice per region, n = 16 mice in total).

The LHb is known to receive direct synaptic input from multiple forebrain regions which contribute to distinct aspects of behaviour[22,23]. We hypothesized that excitatory synaptic input from some of these regions may drive LHb activity during the deliberation period in our risky decision-making paradigm. To evaluate anatomical connectivity of the LHb, we first employed retrograde adeno-associated virus (AAV) labelling of LHb inputs, whole-brain tissue clearing, and 3D light-sheet microscopy (Extended Data Fig. 5a-e). Among the labeled areas were brain regions known to contribute to valence encoding and decision-making processes[28-34], such as the orbitofrontal cortex (OFC), areas of the medial prefrontal cortex (mPFC), the ventral pallidum (VP), as well as the lateral and medial hypothalamus (LH and MH). To verify that these regions indeed send excitatory axonal projections to the LHb, we injected anterograde viral labels into Vglut2-Cre mice. We found strong axonal labeling in the LHb from VP, LH, and MH injections, whereas the axonal

projections from OFC and mPFC seem to rather target the adjacent centrolateral and mediodorsal thalamic nuclei (Extended Data Fig. 5f,g).

To examine how neuronal populations in the candidate input regions functionally couple to the LHb during our task, we next employed multi-fiber photometry in Vglut2-Cre mice and recorded task-related activity in the LHb and simultaneously in 1-2 input regions (Fig. 2f,g; Methods). Based on the anatomical findings, we expected VP, MH, LH to couple most strongly to the LHb. Indeed, population activity in LH and MH yielded the highest single-trial correlation with LHb activity during the deliberation period. Interestingly, while LH-LHb coupling was similar for preferred and non-preferred choices, MH-LHb coupling was lower for the non-preferred option, indicating potentially diverging functions of these two glutamatergic synaptic inputs (Fig. 2h,i). VP showed some coupling to LHb, albeit weaker than for the hypothalamic inputs, whereas mPFC and OFC were rather uncoupled, consistent with the anterograde labeling results.

Next, we examined the behavioural relevance of glutamatergic LHb-projecting neuron activity in LH and MH during the deliberation period. To selectively inhibit LHb-projecting populations, we bilaterally injected a retrograde AAV encoding Cre-dependent Flp-recombinase in the LHb of Vglut2-Cre mice and expressed a Flp-dependent variant of the proton-pump ArchT or EYFP in both hemispheres in either LH or MH (Fig. 3a; n = 8 mice for each region; n = 6 additional mice for each region with EYFP expression as controls). Subsequently, we randomly activated ArchT during the deliberation period in 25% of trials and compared decision-making parameters within perturbation sessions (light ON vs. OFF trials) and across sessions (with vs. without light stimulation sessions; Fig. 3b; Methods). Within perturbation sessions, light stimulation significantly decreased the animals' decision confidence as well as their risk preference levels for activation of MH→LHb neurons but not LH→LHb neurons (Fig. 3c,d). Across sessions, decision confidence decreased in sessions with MH→LHb inhibition (Fig. 3e,f). Finally, preference levels were less stable across sessions, with a significant decrease for LH→LHb inhibition and a decreasing trend for MH→LHb inhibition (Fig. 3g,h). These findings indicate that both

hypothalamic inputs are required for risk preference-selective behavior but that they convey distinct information to the LHb.

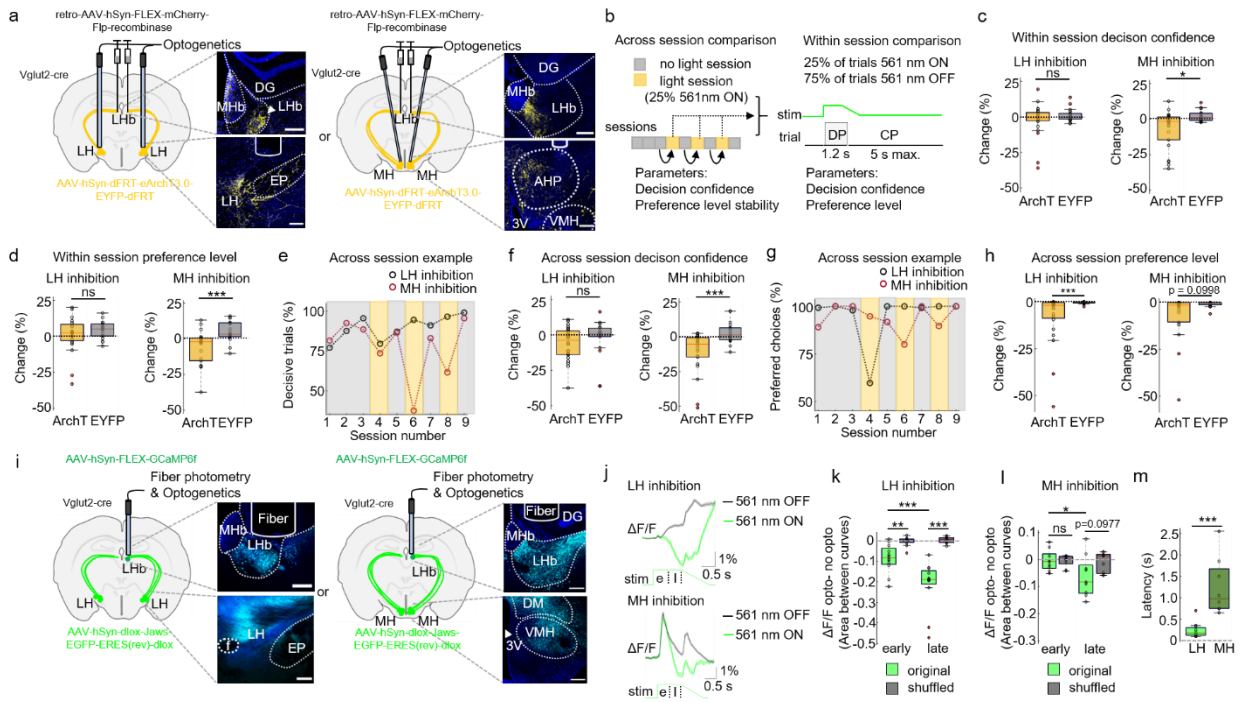

Fig. 3 | Distinct excitatory LHb-projecting hypothalamic regions alter risky decision-making. a, Methodology for optogenetic inhibition of LH→LHb and MH→LHb projection neurons. Histology images are shown for two ArchT-expressing mice. Scale bars 200 µm. **b**, Optogenetic perturbation protocol for across- or within-session comparisons. Labels indicate deliberation (DP) and choice period (CP). **c** and **d**, Within-session comparison of changes in decision confidence (c) and preference level (d) for ArchT-expressing mice (amber) and EYFP-expressing control mice (grey) for LH→LHb and MH→LHb projection neurons. **e,** Decision confidence per session for an ArchT-expressing example mouse for LH→LHb (black) and MH→LHb (red) projection neurons. Amber bars – with illumination, grey bars – without illumination. **f**, Across-session comparison of changes in decision confidence for LH (left) and MH (right) inhibition. **g,** Percentage of preferred choices for an example mouse as in (e). **h**, Across-session comparison of choice stability for LH (left) and MH (right) inhibition (LH: 24 sessions from 8 ArchT mice, 18 sessions from 6 EYFP mice; MH: 22 sessions from 8 ArchT mice and 18 sessions from 6 EYFP mice). All data presented as mean ± s.e.m. **i**, Illustration of hybrid photometry/optogenetics experiment for either LH or MH axonal perturbation. Whereas LHb neurons express Cre-dependent GCaMP6f cytosolically, the Jaws-EGFP fusion protein is membrane-bound and thus leads to more diffuse labeling. **j**, Example photometric calcium traces in LHb from mice with axonal silencing of LH→LHb (top) and MH→LHb (bottom) axons. Green traces with optogenetic axonal inhibition, grey trace without. Data plotted as mean ± 95% c.i. Laser stimulation protocols shown below. Labels indicate early ('e', 0-0.5 s) and late ('l', 0.5-1 s) stimulation phase. **k** and **l**, Differences (with minus without inhibition) of photometric ΔF/F integrals in early and late window for original (green) and shuffled (grey) data for LH→LHb (k) and MH→LHb axons (l). **m**, Latency to the onset of ΔF/F drop below pre-stimulation baseline for LH→LHb and MH→LHb axons (data from 12 sessions in 4 mice for LH and 9 sessions in 3 mice for MH. *p<0.05, **p<0.01, ***p < 0.001, Wilcoxon rank sum test (unpaired) for behavioural data; Wilcoxon signed rank test (paired) or Wilcoxon rank sum test (unpaired) for photometry data. Exact p-values for all figures are provided in Extended Data Table 2.

To further test whether hypothalamic inputs drive LHb population activity prior to action selection, we combined optogenetic inhibition of LH or MH axons in LHb with simultaneous recording of LHb population activity. We bilaterally injected a Cre-dependent version of the chloride-pump Jaws in either LH or MH and recorded LHb population calcium signals with fiber photometry with and without Jaws stimulation (Fig. 3i,j). For both LH and MH axonal projections, activation of Jaws in LHb during the deliberation period significantly reduced LHb calcium signals (Fig. 3k,l; decrement in $\Delta F/F$ integral: LH: -0.08 ± 0.02 %·s, early, -0.19 ± 0.30 %·s, late; MH: -0.004 ± 0.025 %·s early, -0.08 ± 0.01 %·s late; median ± s.e.m.). Whereas inactivation of LH axons rapidly induced a drop in LHb bulk fluorescence, the impact of MH axonal silencing was initially less prominent and occurred with a delay (Fig. 3m; onsets of drop: 0.18 ± 0.05 s in LH and 0.98 ± 0.24 s in MH, median ± s.e.m.). These results indicate that LHb activity depends differentially on synaptic inputs from MH vs. LH in the early vs. late phase of the deliberation period.

Finally, we aimed to scrutinize how risk preference is encoded in LHb on the level of individual neurons and how the distinct hypothalamic inputs influence LHb neuronal representations. We expressed Flp-dependent inhibitory Designer Receptors Exclusively Activated by Designer Drugs (DREADDs) in retrogradely labelled LHb-projecting Vglut2-positive neurons in LH or MH, and longitudinally imaged LHb neurons through an implanted gradient index (GRIN) lens with two-photon microscopy (Fig. 4a). About two thirds of recorded LHb neurons significantly altered their activity during the deliberation period, compared to the pre-cue baseline period (Fig. 4b-d). Of these responsive cells, 60% showed diverging activity during the deliberation period reflecting the animal's subsequent choice of its preferred or non-preferred option (Fig. 4c). We refer to these cells as 'risk-preference-selective cells' (RPSCs). Whereas most RPSCs showed higher activity for the preferred option ('positive' RPSCs), a minority displayed higher mean calcium signals for the non-preferred option ('negative' RPSCs; Fig. 4e; quantified with a risk-preference selectivity

index, RPSI, Methods). These results are consistent with our recordings on the population level (Fig. 2c,d; Extended Data Fig. 4).

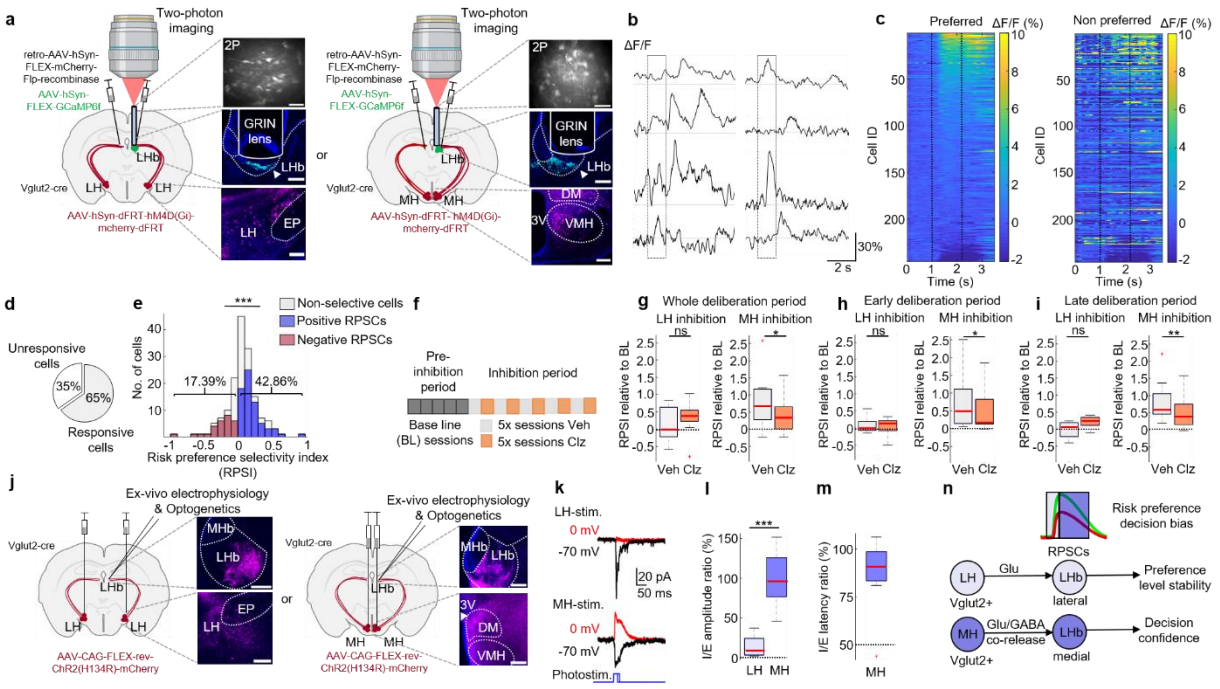

Fig. 4 | MH projections control selectivity of risk-preference-selective LHb neurons during deliberation. a Illustration of two-photon imaging through a GRIN lens combined with cell-type and projection-specific chemogenetic perturbation of LH→LHb and MH→LHb projections (n = 3 mice each). Example images from two animals. Scale bars 200 µm. **b**, Single-trial smoothed traces from example cells across different mice. Box indicates deliberation period. **c**, Mean calcium transients for preferred and non-preferred choice trials. Smoothed data, 247 cells pooled across 6 mice, sorted for mean activity in the deliberation window of preferred choice trials. Dashed lines indicate onset of start and reward cue. **d**, Fraction of cells responsive during the deliberation period (grey). **e**, Responsive cells sorted by risk preference selectivity index (RPSI). **f**, Chemogenetic perturbation protocol. Baseline (BL) sessions with no injection (dark grey), vehicle injection (Veh; light grey), and clozapine (Clz; light orange). **g-i**, BL-normalized RPSI of risk preference selective cells (RPSCs) for Veh and Clz sessions for whole (**g**), early (**h**), and late (**i**) deliberation period. **j**, Illustration of ex vivo whole-cell recordings in brain slices with cell-type specific optogenetic stimulation of LH→LHb or MH→LHb axons. **k**, Example current traces of excitatory and inhibitory postsynaptic currents (EPSC, black, -70 mV holding potential; IPSC, red, 0 mV holding potential) evoked by photostimulation (blue) of LH→LHb (top) and MH→LHb (bottom) axons. **l**, Ratio of photostimulation-evoked IPSC/EPSC amplitudes. **m**, Latency ratio for IPSC vs. EPSC (8 cells in 4 mice for MH axons; 9 cells in 4 mice for LH axons). **n**, Working model of parallel hypothalamic-lateral habenula circuits in encoding of risk preference decision bias. Traces indicate LHb RPSCs activity during deliberation for preferred (green) and non-preferred (red) option. Coloured boxes indicate proposed activation windows of LH→LHb (light blue) and MH→LHb (deep blue) inputs. *p<0.05, **p<0.01, ***p < 0.001, χ^2-test, Wilcoxon signed rank test (paired) or Wilcoxon rank sum test (unpaired).

Next, we aimed to uncover how distinct hypothalamic inputs influence risk-preference selectivity of RPSCs. We identified RPSCs based on their activity in five baseline sessions and compared their selectivity relative to baseline with (clozapine injection, Clz) and without (vehicle injection,

Veh) chemogenetic inhibition of Vglut2-positive LH→LHb or MH→LHb projection neurons (Fig. 4f; Methods). Inhibition of MH→LHb but not LH→LHb neurons decreased risk-preference selectivity of RPSCs during the deliberation period (Fig. 4g; RSPI changes: 0.003 ± 0.14 and 0.39 ± 0.12 for Veh vs. Clz for LH; 0.70 ± 0.25 and 0.38 ± 0.17 Veh vs. Clz for MH; median ± s.e.m; see Extended Data Fig. 6 for Clz-only controls). Based on the time course of the effect of silencing MH→LHb axons on LHb acitivity (Fig. 3l,m), we further compared effects of inhibition in the early and late phase of the deliberation period. During the late phase, the effects of MH inhibition were even more robust than in the early phase (Fig. 4h,i; RPSI changes: Late, 0.07 ± 0.09 and 0.26 ± 0.06 Veh vs. Clz for LH; 0.58 ± 0.16 and 0.36 ± 0.14 Veh vs. Clz for MH; Early, 0.013 ± 0.06 and 0.16 ± 0.07 Veh vs. Clz for LH; 0.48 ± 0.27 and 0.19 ± 0.21 Veh vs. Clz for MH). A decrease in risk-preference selectivity was further observed in a subpopulation of LHb RPSCs when mice shifted their preference to the alternative option in response to expected value changes (Extended Data Fig. 7). However, most LHb RPSCs switched their risk-preference selectivity during deliberation once the new preference was established, indicating that LHb activity flexibly adapts to value-based changes in risk preference.

These results tempted us to ask how Vglut2-positive LHb-projecting neurons in the LH and MH might exert such different influence on LHb neurons. To address this question, we expressed Cre-dependent channelrhodopsin-2 (ChR2) either in LH or MH of Vglut2-Cre mice and performed ex-vivo whole-cell recordings from LHb neurons in acute brain slices. We stimulated the ChR2-expressing axonal projections with light and measured the light-evoked synaptic currents in LHb neurons (Fig. 4j). Both LH→LHb and MH→LHb projections showed high connectivity with LHb neurons, as evidenced by light-evoked excitatory post-synaptic currents (EPSCs) (Fig. 4k; Extended Data Fig. 8a,b). Intriguingly, stimulation of MH→LHb axons, but not LH→LHb axons, also elicited prominent inhibitory post-synaptic currents (IPSCs) (Fig. 4k,l). MH-evoked EPSCs and IPSCs occurred with similar onset latencies (Fig. 4m; I/E latency ratio, 91 ± 62%), persisted

under conditions of polysynaptic blockade (tetrodotoxin with 4-aminopyridine) and were sensitive to glutamate (Glu) receptor and $GABA_A$ receptor antagonists (Extended Data Fig. 8c). These findings suggest that Vglut2-positive MH→LHb neurons co-release Glu and GABA in the LHb, whereas Vglut2-positive LH→LHb neurons appear to release Glu exclusively[34]. Such Glu/GABA co-release from MH→LHb axon terminals might enable fine-tuned gain control[13] over the activity of LHb RPSCs during the late deliberation period, setting a stable risk-preference bias that promotes more confident decisions.

Discussion

In this study we applied a balanced two-alternative choice task to test risky decision-making in head-fixed mice. Most mice displayed strong and stable choice-preference traits, with the majority of individuals exhibiting probabilistic discounting as well as prominent risk aversion, as has been observed in various other species[1-5,7,8,35]. In a previous study, pharmacological inactivation of the LHb impaired discounting behaviour by preventing the formation of value-based preferences[9]. Here, we investigated how LHb neuronal activity encodes risk preference and the timing of behaviourally relevant LHb activity. We found that LHb activity patterns reflect individual risk preferences during choice deliberation, both at the population level and with cellular resolution. A subset of risk-preference-selective LHb cells encodes individual risk preference even on the single-cell level, by displaying diverging activity for the individually preferred and non-preferred choice options. In most cells the activity was higher for the preferred choice option. Such 'positive' encoding of a preference is particularly remarkable given that increased LHb activity has largely been associated with negative valence signalling in aversive contexts[10,11,36,37]. On the other hand, our findings are in line with other studies that found a subset of LHb neurons increase their activity during reward anticipation[38,39].

Furthermore, we identified two long-range hypothalamic projections providing excitatory inputs (and inhibitory for MH) that influenced LHb activity, both on the population as well as the single-

cell level bearing behavioural relevance for risky decision-making. LH→LHb projections previously were shown to modulate behaviour in aversive settings[22,34,40] but not reward-driven behaviours. MH→LHb projections have been described anatomically[41] but have not been functionally examined so far. Interestingly, we did not observe direct anatomical input connections or correlated activity of LHb neurons with excitatory neurons in the orbitofrontal or medial prefrontal areas, indicating that these neuronal populations might not exert their function via direct projections to the LHb. Moreover, we cannot rule out influences of other input areas or of non-excitatory populations. Indeed, inhibitory synaptic inputs to the LHb have recently been shown to be required for reward anticipation[39].

Based on our anatomical (Fig. 4j, Extended Data Fig. 5g) and functional data we constructed a schematic of two parallel hypothalamic-habenula pathways (Fig. 4n). Whereas LH→LHb inputs mainly target lateral pools of LHb RPSCs, providing excitatory drive to stabilize choices across time, MH→LHb inputs innervate more medial LHb RPSCs, increasing decision confidence by setting the risk-preference bias via Glu/GABA co-release. Our proposed circuit of parallel hypothalamic-habenula input pathways is further supported by the organization of LHb outputs. LHb projection neurons send direct, marginally overlapping axonal projections to dopaminergic and serotonergic neuromodulator systems in the ventral tegmental area (VTA), the medial raphe nucleus (MRN), and the dorsal raphe nucleus (DRN)[21,23,42,43]. Since these regions fulfill distinct functions in value-guided behaviours, we may propose that distinct hypothalamic-habenula inputs contribute to these functions. Taken together, this study shows that evolutionary conserved brain regions form highly specific neuronal circuits to fulfill distinct functions in habitual value-based decision-making processes.

Methods

All experimental procedures were carried out in accordance with the guidelines of the Federal Veterinary Office of Switzerland and were approved by the Cantonal Veterinary Office in Zurich under license number 234/2018 and 153/2019.

Animals. A total of 101 male and 12 female adult mice were used in this study. Mice were maintained on a reversed 12:12 light dark cycle and tested during the dark phase. For behavioural training we used C57BL6/J mice and Vglut2-ires-Cre mice (Jackson Laboratories, no. 016963). For fiber photometry, optogenetic perturbation, two-photon experiments, *ex vivo* electrophysiology, and anterograde tracing we used Vglut2-ires-Cre mice (80 mice). For *in vivo* electrophysiology and behavioural analysis we used C57BL6/J mice (26 mice). For tissue clearing we used ai14-tdtomato mice (Jackson Laboratories, no. 007908; 7 mice).

Behavioural training. We trained animals in the balanced two-alternative choice task. On the first day of training, mice were shaped to sample both spouts using 2.5-µl sucrose rewards which were automatically delivered. Once the animals successfully learned to sample both spouts for reward, auto-reward was abandoned, and the spouts would deliver 2.5-µl rewards only upon licking after the reward cues. When mice learned this association and continued to sample both spouts, we would introduce free-choice sampling on day 2-3. Mice first performed 50 trials of forced choice, followed by 200-300 free choice trials where both spouts delivered the same reward quantity of 2.5 µl. After this initial training phase, different reward quantities were introduced to examine individual preferences. The ‘safe’ spout delivered a reward of 5 µl sucrose water in 100% of all cases, whereas the ‘risky’ spout either delivered 17 µl in 25% or 1 µl in 75% of cases. Hence the expected value was equal for the two waterspouts. If not indicated otherwise, every mouse performed 50 forced choice trials where only one spout provided a reward with a maximum of 3 repetitions of the same option, followed by 200-300 free choice trials where the animal could freely decide which spout to sample and both spouts carried a potential reward. Start of the trial and end of the deliberation period were signaled by a 6 kHz auditory tone. Potential reward location was indicated by an LED light close to the respective spout, i.e., on one side in forced choice trials and on both sides for free choices. To exclude learning effects, mice were trained until their behavioural performance varied by less than 20% across more than three consecutive training days. Subsequently, every animal absolved additional 14 daily sessions consisting of 50 forced-choice and 200-300 free-choice trials. Mice required 2.53 ± 0.54 sessions (mean ± s.e.m., n = 45) before reaching stable performance levels. Moreover, mice were required to indicate a clear decision in more than 50% of all free choice trials (decision confidence > 50%).

A trial was labelled indecisive when an animal sampled both spouts during the deliberation period prior to action selection. Risk preference classification was determined based on the mice's average engagement into risk across all 14 sessions ('risk averse', <25% risky choices; 'risk neutral', between 25%-75%; 'risk prone', >75%). These criteria were established by prior experimentation.

To test the mice's ability to measure expected value difference between spouts, we trained another seven mice until they reached stable baseline performance and then altered the expected value of the safe spout (Extended Data. Fig. 1). Mice were trained until reaching a stable performance level before the expected value was further changed. During these expected-value control experiments animals performed 50 forced-choice and 200 free-choice trials per daily session.

Body movement and pupil diameter measurements. Behaviour was assessed in a sound-isolated box to shield the animals from external cues, except for two-photon imaging experiments (but with the microscope shielded from all sides). For assessment of general locomotor activity, we recorded the animals' posture during the entire trial period with a frame rate of 30 Hz using an infra-red sensitive body camera (DMK23UP1300; The Imaging Source). To detect general body movements, we outlined three regions of interest covering the forelimbs, mouth, and neck area, respectively, as described previously[44]. Next, we calculated body movement for each region and trial as 1 minus the frame-to-frame correlation as a function of time for each trial. For correlation with fluorescence data, data were down sampled to 20 Hz.

Behaviour analysis. To understand risk preference behavior in mice, we analysed three main behavioural variables: Decision confidence, fraction of risky choices, and preference level. Decision confidence, *D*, was defined as the ratio of all trials, in which an animal clearly indicated a decision (i.e., 'safe choice', 'risky choice', or 'miss' trials), divided by the total number of trials, T_{tot}:

$$D = \frac{T_{tot} - T_{indec}}{T_{tot}} \quad (1)$$

Where T_{indec} denotes the number of indecisive trials. In the free-choice condition, a trial was labelled 'indecisive' when the animal sampled both spouts during the deliberation period prior to action selection (and as a 'miss' if the animal did not lick at all). The fraction of risky choice, FRC, was defined as the ratio of all risky trials by the total number of all decisive trials:

$$FRC = \frac{T_{risky}}{T_{decisive}} \quad (2)$$

The preference level, PL, either for the safe or risky option was defined as the ratio of all preferred choice trials, T_{pref}, by the total number of all decisive trials:

$$PL = \frac{T_{pref}}{T_{decisive}} \tag{3}$$

Behavioural modeling of choices was performed to better understand the history-dependence of risky or safe choices for each mouse. Modeling comprised four possible choices (risky choice, safe choice, indecisive, miss) and five possible outcomes (risky loss, risky win, safe, indecisive, miss). Transition matrices (Fig. 1d) describe the Markovian transition probabilities from the previous trial's outcome to the current trial's choice and were normalized such that the sum across all choices for a given outcome equaled to 1. To compare transition matrices across mice (Fig. 1e), the 4 x 5 transition matrix for each mouse was interpreted as a vector with 20 values and compared with transition matrices from other mice using Pearson's correlation coefficient.

To investigate the history-dependence of choices for multiple preceding trials, we applied multinomial linear regression with the mnrfit() function in MATLAB, using the past outcomes to predict the current decision. The categorical variables used for regression were the possible decisions ('safe choice', 'miss', 'indecisive', 'risky choice'), while the possible outcomes of the previous trials ('safe choice', 'miss', 'indecisive', 'risky choice/loose', 'risky choice/win') were used as regressors. To prevent overfitting, we used five-fold cross-validation. To quantify model performance, we computed a loss function that is used as standard for categorical variables ('cross-entropy loss') and computed the median performance across cross-validated subsets for each mouse. The loss function as a function of previous trials was normalized for each mouse by subtracting the minimum of the loss function. Plots in Extended Data Fig. 2 show the negative of this normalized loss as the final performance metric.

Elevated plus maze test. After completion of behavioural training, animals were tested for anxiety levels in an elevated plus maze test. The maze consisted of two orthogonal open and closed arms (30 cm each) and a center zone (6 cm), elevated 110 cm above the ground. Mice were allowed to freely explore the maze for 5 min. Video images were acquired at 30 Hz from a camera (DMK23UP1300; The Imaging Source) mounted 100 cm above the maze. To compute the time spent in open and closed arms, semi-automated video analysis was performed. A simple threshold-based segmentation algorithm (custom-written in MATLAB) was applied to the background-subtracted video in order to identify the pixels associated with the largest non-background object, i.e., the mouse. Prior to automated analysis of the full video, the threshold

was manually adjusted for each video based on interactive inspection of the segmented movie together with the raw movie. From this segmented object, the fractions of object pixels in open or closed arms or the center square of the plus maze were computed.

Virus injections. Before surgery, mice were briefly anesthetized with isoflurane (2%) in oxygen in an anesthesia chamber. Afterwards, animals were head-fixed in a stereotactic frame (Kopf Instruments) while anesthesia was maintained with 1-1.5% isoflurane. Body temperature was maintained at ~37°C using a heating pad with a rectal thermal probe. To avoid dry eyes, the mouse's eyes were covered with a vitamin A cream (Busch &Lomb). To prevent pain and inflammation, mice were subcutaneously injected with 0.1 µl/g body weight meloxicam. After longitudinal incision, connective tissue was removed, and the skull was dried using absorbent swabs (Sugi; Kettenbach).To target our regions of interest we used the following coordinates (from the brain surface): medial orbital frontal cortex (mOFC, bregma (B): +2.80 mm, lateral (L): 0.2 mm, ventral (V): 1.2 mm), medial prefrontal cortex (mPFC, BLV: +1.70 mm, 0.2 mm, 1.2 mm), ventral pallidum (VP, BLV: +0.75 mm, 1.5 mm, 4.5 mm), medial hypothalamus (MH, BLV: -1.20 mm, 0.5 mm, 4.7 mm), lateral hypothalamus (LH, BLV: -1.30 mm, 1.6 mm, 3.6 mm), and lateral habenula (LHb, BLV: -1.70 mm, 0.5 mm, 2.5 mm). We used the following viral constructs and injection volumes per site in the different types of experiments: AAV.9.Syn.Flex.GCaMP6f.WPRE.SV40 (calcium recordings 140 nl; Addgene, no. 100833); AAV.1.hSyn.dio.EGFP (anterograde labelling, 140 nl, Addgene, no. 50457); retrograde.AAV.hSyn1.chI.mCherry.2A.iCre.WPRE.SV40p (retrograde labelling of LHb inputs and whole-brain clearing, 70 nl, Viral Vector Facility of the University of Zurich [VVF], no. v147), retrograde.AAV.hSyn1.chI.dlox.mCherry.2A.NLS.FLPo(rev).dlox.WPRE.SV40p(A) (cell-type specific retrograde labelling, 140 nl, VVF, no. v173), ssAAV1.2.hSyn1.chI.dFRT.eArchT3.0.EYFP.dFRT.WPRE.hGHp(A) (optogenetics, 140 nl, VVF, no. v423), ssAAV.5.2.hSyn1.dlox.Jaws.KGC.EGFP.ERES(rev).dlox.WPRE.bGHp(A).SV40p(A) (optogenetics, 140 nl, VVF, no. v508), AAV.9.FLEX.rev.ChR2(H134R).mCherry (optogenetics, 140 nl, Addgene, no. 18916), AAV.9.Ef1A.fDIO.EYFP (control for optogenetics, 140 nl, Addgene, no55641), ssAAV.1.2.hSyn1.dFRT.hM4D(Gi).mCherry(rev).dFRT.WPRE.hGHp(A) (chemogenetics, 140 nl, VVF, no. v190).

Fiber and GRIN lens implantation. Upon removal of skin and connective tissue, iBond (Kulzer, Total Etch) was applied to the clean skull and cured by UV light. Subsequently, a slim ring of Charisma (Kulzer, A1) was sculpted, and UV cured at the edge of the exposed skull to optimize implant stability. Small craniotomies were drilled above the regions of interest. Fiber implants or

600-µm gradient index (GRIN) lens (Inscopix) were slowly lowered right above the respective regions using custom-made holders and fixed in place using UV cured dental cement. Fiber implants consisted of an optical fiber (200-µm or 400-µm core) attached to a metal ferrule (Thorlabs).

Fiber photometry. Fiber photometry recordings were performed with a custom-built setup that allowed simultaneous recording of three channels in parallel. For excitation we used an Omicron LuxX 473-nm laser, modulated at 490 Hz. Laser light was attenuated with a neutral density filter (NDC-25C-4M, Thorlabs) and split twice using non-polarizing beam splitters (CCM1-BS013/M, Thorlabs). For detection we used photomultiplier tubes (Hamamatsu). Fluorescence emission was recorded at 2 kHz and downsampled to 20 Hz for analysis. Excitation and emission light were transmitted through the same multimode fiber (UM22-200 and UM22-400, NA = 0.22; Thorlabs). For combination of fiber photometric recordings with optogenetic perturbation, 561-nm laser light (Coherent, OBIS) was coupled into the light path of one channel.

Optogenetics. For optogenetic perturbation, we used a Cre-dependent version of the chloride pump Jaws as well as a Flp-dependent version of the proton pump ArchT. To assess stable baseline performance prior to optogenetic intervention, multiple baseline sessions without opsin activation were recorded. Both opsins were activated using 561-nm laser light (OBIS laser; Coherent). To circumvent excessive tissue heating[45] as well as rebound activation[26,46], low intensity laser light (5-6 mW at the fiber tip) was modulated at 40 Hz and ramped down for 1 s. Moreover, perturbation was randomly applied in a maximum of 25% of trials within a session. Every perturbation session was followed by a session without opsin activation (non-perturbation session).

We compared decision confidence and preference level within a perturbation session as well as decision confidence and preference level stability between perturbation and a non-perturbation session. We evaluated the following changes for light ON compared to light OFF trials:

Decision confidence change: $D_{on} - D_{off}$ (in %) (4)

Preference level change: $PL_{on} - PL_{off}$ (in %) (5)

These changes were compared between EYFP-expressing and ArchT-expressing mice.

Chemogenetics. For chemogenetic perturbation, we used a Flp-dependent version of inhibitory DREADDs hM4D(Gi). To assess stable baseline performance prior to DREADDs intervention, multiple baseline sessions without injection were recorded over several days before intraperitoneal injections of vehicle or clozapine were introduced. The DREADD receptor was

activated by intraperitoneal injection of clozapine (0.005mg/kg; Tocris) 5-10 minutes prior to the start of the experiment[47,48]. Vehicle (5 mM ascorbic acid in Ringer solution) and clozapine were administered alternately in consecutive daily sessions.

***In vivo* electrophysiology.** Chronic electrophysiological recordings were performed in four wild-type (C57BL/6) male mice. During the initial surgery, the scalp was retracted, the skull was exposed and the implantation target was marked with a permanent marker before sealing the skull with dental acrylic and positioning a headpost over the cerebellum. Mice were subsequently allowed to recover for 7 days before they were handled and acclimatized to the behavioural setup and trained on the task. In a second surgery, the mice were anesthetized as previously and a silicon linear electrode array (16 sites, 20-μm inter-electrode distance; Atlas Neurotechnologies) was targeted to the LHb. The linear array was dipped in a lipophilic dye (DiI; Sigma-Aldrich) for subsequent localization. A small craniotomy (~0.75 mm) was performed above the target and two additional trepanations (~0.2 mm) were performed over the cerebellum and the frontal cortex for placement of ground and reference electrodes. Next, the probe was slowly inserted centering the electrode sites in the LHb. After implantation the probe was fixed in place with additional acrylic and silver wires placed in contact with the cerebrospinal fluid (CSF) to serve as ground and reference electrodes. The mice were allowed to recover for another 5 days after surgery and their health was monitored. Mice were placed in an enclosed, sound-proof box and head-fixed during performance of the task. Electrophysiological recordings were performed while the mice performed the task. The voltage from the electrode array was amplified and digitally sampled at a rate of 30 kHz using a commercial extracellular recording system (Intan). The raw voltage traces were filtered off-line to separate the multiunit activity (MUA) (band-pass filter 0.6–6 kHz) using a fifth-order Butterworth filter. Subsequently, for each electrode a threshold was applied to the high-pass filtered data to isolate multiunit activity and reject background noise (4 times the standard deviation across the recording session, specified per electrode). To combine firing rates across units and animals, the firing rates in time windows of interest were z-scored by using the pre-task firing rate as a baseline. The MUA was subsequently downsampled to the sampling rate of the fiber photometry (20 Hz) to compare the population time course with the bulk photometry signal.

***In vitro* electrophysiology.** Whole-cell patch-clamp electrophysiological recordings were obtained in LHb-containing acute brain slices prepared from adult mice. Coronal brain slices were prepared in cold choline cutting solution containing (in mM): 100 choline chloride, 25 $NaHCO_3$, 25 D-glucose, 2.5 KCl, 7 $MgCl_2$, 0.5 $CaCl_2$ and 1.25 NaH_2PO_4, aerated with 95% O_2 / 5% CO_2. Slices were perfused at a rate of 0.5–1 ml/min with oxygenated artificial CSF (aCSF) containing (in mM):

128 NaCl, 26 $NaHCO_3$, 10 D-glucose, 3 KCl, 1 $MgCl_2$, 2 $CaCl_2$ and 1.25 NaH_2PO_4, aerated with 95% O_2 / 5% CO_2 at 29ºC. Patch electrodes were made from borosilicate glass (Harvard Apparatus) and had a resistance of 2-4 MΩ. The intracellular solution contained (in mM): 126 cesium methanesulfonate, 4 CsCl, 10 HEPES, 20 phosphocreatine, 4 MgATP, 0.3 NaGTP, pH 7.3, 290 mOsm. Experiments were performed in voltage-clamp mode using the Axopatch 200B amplifier (Molecular Devices). Visually-guided whole-cell recordings were obtained of cells in a field of fluorescent axons (from ChR2(H134R)-mCherry injection into LH or MH) on a Zeiss Axioscope using an optiMOS camera (Q Imaging). Access resistance was monitored to ensure the stability of recording conditions. Recordings with access resistance >40 MΩ or whole cell capacitance <4 pF were excluded. No compensation was made for access resistance and no correction was made for the junction potential between the pipette and the ACSF. Following a baseline stabilization period (2-3 min), electrically isolated excitatory or inhibitory postsynaptic currents were evoked by photostimulation (488 nm) at holding membrane potentials of V_h = -70 mV and V_h = 0 mV, respectively. Nine recurring photostimuli of sequentially increasing length (20 to 250 ms) were delivered at 0.2 Hz with a Polygon400 (Mightex), localized to the soma of the recorded cells. An average of 30 sweeps were analyzed for each condition from each cell using Clampfit10 (Molecular Devices). Bath applied compounds TTX (1 µM, Tocris 1069, CAS: 18660-81-6), 4-AP (100 µM, Tocris, 0940, CAS: 504-24-5), CNQX (20 µM, Tocris, 1045, CAS: 479347-85-8), D-APV (100 µM, Tocris, 0106, CAS: 79055-68-8), or gabazine (25 µM, Tocris, 1262, CAS: 104104-50-9) were dissolved as stock solutions in water. For quantification, current peak amplitude was calculated as an average of 3 ms surrounding the first evoked peak. Onset delay was measured as the average time to initial deflection from stimulus onset. Average spiking was calculated as the average spike rate of 2x 20-ms windows prior to (pre-stim.) and during (stim.) optogenetic stimulation.

Two-photon calcium imaging. Two-photon calcium imaging data were acquired with a custom-built two-photon microscope controlled by ScanImage (Basic Version; Vidrio Technologies LLC, Ashburn), equipped with a Ti:sapphire laser system (approximately 100-fs laser pulses, center wavelength 910 nm; Mai Tai HP, Newport Spectra Physics), a Pockels cell for intensity modulation (Conoptics), a laser scanning unit with an 8-kHz resonant scan mirror (Cambridge Technology) and a galvanometric mirror (6215H, Cambridge Technology), and a 20x air objective (N Plan L 566035, NA = 0.40; Leica). Imaging was performed through the implanted GRIN lens (500-µm diameter, ~6.1 mm length, 1050-004599, Inscopix). Fluorescence signal was detected with a photomultiplier tube (Hamamatsu) after passing through an IR blocking filter. Images were acquired at 30 Hz with 512x512 pixel resolution. Laser power was adjusted to 30 mW under the

objective. Single trials (8.2 – 12.7 s long) were recorded with breaks of 0.5 s during the inter-trial period to allow data saving. To ensure two-photon signal integrity during the two-alternative choice task, LED signalling was omitted in these experiments and the reward cue solely consisted of the 6-kHz auditory tone.

Source extraction and quality control of calcium imaging data. Raw data were corrected for brain motion using a modified version of rigid movement correction based on phase correlation (Suite2p)[49]. Under the GRIN lens, the illumination profile is highly inhomogeneous across the field of view (FOV), with higher intensity in the center of the FOV and lower intensity at the edges. To avoid brain motion artifacts due to the illumination profile that moved by the same amount, we estimated the illumination profile by smoothing the average fluorescence image with a 2D median filter (100-pixel size). We divided each raw movie frame by this illumination template, performed rigid movement correction, and then multiplied each corrected movie frame with the illumination template. For source extraction, a trial-averaged movie was generated for each session and used to manually draw regions of interest (ROIs) around active neurons[50]. Neuronal ROIs were manually mapped across session based on visual inspection of the mean fluorescence image, and discarded if the respective ROI had moved out of focus for a new session. ROIs were drawn based on anatomical features visible in the average fluorescence image, but also based on maps of local correlations[51]. Potential residual movement artifacts were identified by inspection of the map of local correlations. Movement artifacts were usually visible as anti-correlated left/right or top/bottom borders of a single neuron. To rule out motion artifacts from a second perspective, trial-averaged movies and single-trial movies were visually inspected together with the extracted traces. Mice for which movement artifacts could not be eliminated, e.g. due to excessive axial brain motion, were excluded from the analysis.

Calcium imaging data analysis and functional classification. Calcium transient time series data were extracted and analysed using custom MATLAB code. $\Delta F/F$ was calculated on a trial-by-trial basis for each ROI as: $(F - F_0)/F_0$, where baseline F_0 is the average signal over the last second of the inter-trial interval before the next trial starts with the auditory starting cue. To identify responsive neurons that show a significant increase or decrease in fluorescence signal during the deliberation period, we compared the mean calcium activity of the last second of the inter-trial interval with the mean calcium activity of the deliberation period (Wilcoxon signed rank test, significance threshold of $p<0.05$).

To identify the ‘risk-preference-selective cells’ (RPSCs) amongst all responsive cells, we first calculated the area under the curve (AUC) for $\Delta F/F$ traces during the deliberation period for

preferred and non-preferred choice trials. We then calculated the risk-preference selectivity index, RPSI, based on the mean AUC values (AUC_{pref} and AUC_{nonpref}, respectively) according to:

$$RPSI = \frac{AUC_{pref} - AUC_{nonpref}}{AUC_{pref} + AUC_{nonpref}} \quad (6)$$

We normalized RPSI values by dividing each cell's RPSI by its maximum absolute RPSI:

$$RPSI_{norm} = \frac{RPSI}{|RPSI_{max}|} = \frac{AUC_{pref} - AUC_{nonpref}}{|AUC_{pref} - AUC_{nonpref}|_{max}} \quad (7)$$

A cell was classified as 'risk-preference-selective' when its $RPSI_{norm}$ was at least twice as high as the score calculated from its shuffled data.

For measuring the effect of chemogenetic silencing of hypothalamic inputs on LHb RPSCs, we first identified RPSCs during the last five sessions before vehicle and clozapine injections as described above. Then we tracked these cells across the entire inhibition period and calculated their difference scores. Subsequently we calculated their RPSI by dividing each cells difference score by the maximum difference score detected during the pre-injection baseline period. In the final analysis we included only cells for which the RPSI could be tracked through the entire period.

To evaluate the activity of risk-preference-selective LHb neurons upon preference changes, we recorded at least another five sessions after chemogenetic inhibition as new baseline. Subsequently, we changed the expected value ratio between the two options by sequentially decreasing the value of the preferred and increasing the value of the non-preferred option. We then recorded the cell activity, and calculated risk-preference selectivity indices as described above. Only cells, for which risk-preference selectivity could be tracked throughout the entire period were included in the final analysis.

***Post hoc* immunohistochemistry.** After completion of behavioural training, mice were anesthetized (100 mg/kg and 20 mg/kg xylazine) and perfused transcardially with 4% paraformaldehyde in phosphate buffer, pH 7.4. After perfusion, tissue was removed from the ventral side of the skull bone until the brain was exposed. Subsequently, the exposed brain with the respective implant was additionally post-fixed with 4% paraformaldehyde for 2 to 7 days. After fixation, the brain was carefully separated from the implant. Coronal sections (100 µm thick) were cut with a vibratome (VT100; Leica). Sections were mounted onto glass slides and confocal images were acquired with an Olympus FV1000.

Tissue clearing, light-sheet imaging and data analysis. Brain samples were stained for tdTomato and cleared with a modified version of the iDISCO protocol[52]. After six weeks of

expression, mice were perfused and the brains post-fixed in 4% PFA in PBS for 4.5 hours at 4°C, shaking at 40 rpm. Brains were washed in PBS for three days at RT and 40 rpm, with daily solution exchange. Samples were dehydrated in serial incubations of 20%, 40%, 60%, 80% methanol (MeOH) in ddH_2O, followed by two times 100% MeOH, each for one hour at RT and 40 rpm. Pre-clearing was performed in 33% MeOH in dichloromethane (DCM) overnight (o.n.) at RT and 40 rpm. After two times washing in 100% MeOH each for 1 hour at RT and then 4°C at 40 rpm, bleaching was performed in 5% hydrogen peroxide in MeOH for 20 hours at 4°C and 40 rpm. Samples were rehydrated in serial incubations of 80%, 60%, 40%, and 20% MeOH in in ddH_2O, followed by PBS, each for one hour at RT and 40 rpm. Permeabilization was performed by incubating the mouse brains two times in 0.2% TritonX-100 in PBS each for 1 hour at RT and 40 rpm, followed by incubation in 0.2% TritonX-100 + 10% dimethyl sulfoxide (DMSO) + 2.3% glycine + 0.1% sodium azide (NaN_3) in PBS for three days at 37°C and 65 rpm. Blocking was performed in 0.2% Tween-20 + 0.1% heparine (10 mg/ml) + 5% DMSO + 6% donkey serum in PBS for two days at 37°C and 65 rpm. Samples were stained gradually with primary polyclonal rabbit-anti-RFP antibody (Rockland, 600-401-379-RTU) and secondary donkey-anti-rabbit-Cy3 antibody (Jackson ImmunoResearch, 711-165-152) 1:2000 in 0.2% Tween-20 + 0.1% heparine + 5% DMSO + 0.1% NaN_3 in PBS (staining buffer) in a total volume of 1.5 ml per sample every week for four weeks at 37°C and 65 rpm. Washing steps were performed in staining buffer five times each for one hour, and then for two days at RT and 40 rpm. Clearing was started by dehydrating the samples in serial MeOH incubations as described above. Delipidation was performed in 33% MeOH in DCM o.n. at RT and 40 rpm, followed by two times 100% DCM each for 30 minutes at RT and 40 rpm. Refractive index (RI) matching was achieved in dibenzyl ether (DBE, RI = 1.56) for four hours at RT. 3D stacks of cleared brains and hemispheres were acquired using the mesoSPIM light-sheet microscope[53] at 1X with a resolution of 6 µm/voxel. Imaging data were post-processed by using Fiji (Image J, 1.8.0_172 64 bit) and Imaris (9.8.0, Oxford Instruments), and analysed by using ClearMap2[54] (https://github.com/ChristophKirst). The analysis consisted of three steps: alignment to standard atlas, cell detection, and segmentation into annotated brain areas. Briefly, the autofluorescence channel of cleared brain samples was first aligned to the standard Allen brain atlas (http://www.brain-map.org). Then, potential cells were detected by finding local maxima in the 3D volume. Detected cells were filtered by size with a custom threshold adjusted to each sample. Finally, detected cells were assigned to brain regions based on the annotated brain atlas. All brain samples were manually screened by two experimentalists to ensure the quality of alignment and cell detection, and spurious cell detection from structures with no clear cell labelling is excluded from final analysis.

Statistical analysis Statistical analyses are described in the main text, figure legends, and Extended Data Table 2. We applied parametrical (two-sided t-test) or non-parametrical (Wilcoxon rank sum test, Wilcoxon signed rank test, Chi square test) tests in MATLAB. Significance was assumed as $p<0.05$.

Data availability

Data are available from the authors upon reasonable request.

Code availability

Code is available from the authors upon reasonable request.

Contributions

D.G. conceived the project; D.G. and F.H. designed the study; D.G. carried out all surgeries, behavioural training, and in vivo experiments with the help of Y.S. (fiber photometry), C.L. (multi-unit electrophysiology), and P.R. (two-photon imaging); D.G., P.R., and C.L. analysed behavioural, optical, and *in vivo* electrophysiological data; A.M.R. performed tissue clearing and light-sheet imaging together with D.G.; S.H. and D.G. analysed light-sheet data; T.S. performed and analysed ex vivo brain slice recordings; M.W. designed and wrote the custom behaviour control software; T.K, A.A., and F.H. provided supervision; D.G. and F.H. wrote the manuscript with comments from all authors.

Acknowledgements

This work was support by grants to F.H. from the Swiss National Science Foundation (project grants no. 310030-127091 and 310030_192617; Sinergia grant no. CRSII5-18O316), the European Research Council (ERC Advanced Grant, BRAINCOMPATH, 670757), and to D.G., C.L., and P.R. from the University of Zurich (Forschungskredit grants, projects K-41220-05-01, K-41220-04 and K-41220-06-01). The authors thank Philipp Bethge for managing transgenic mouse lines, Dubravka Dujmovic-Göckeritz for genotyping, Hansjörg Kasper and Stefan Giger for technical support, Philippe Tobler and Manuel Mameli for helpful discussions.

Declaration of interests

The authors declare no competing interests.

Extended Data Figures and Tables

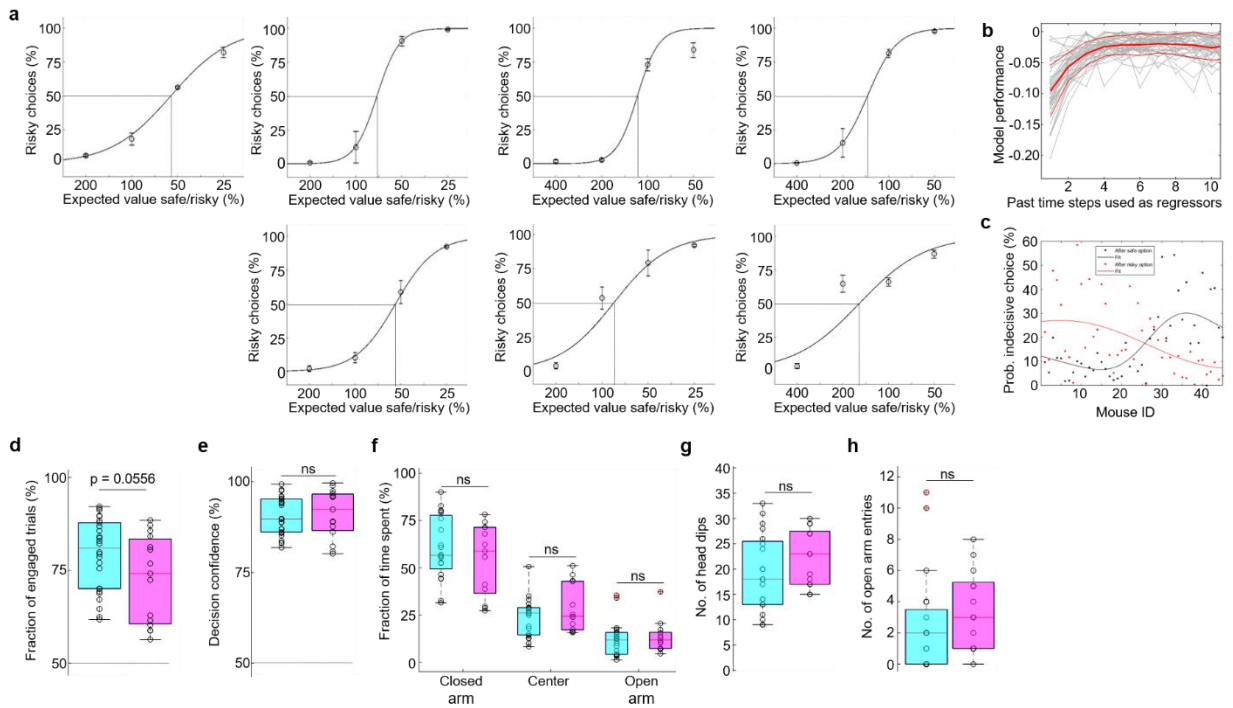

Extended Data Fig. 1 | Mice performing two alternative choice task adapt their choices depending on expected values, choice history, motivation but not anxiety level. a, Every plot represents data from an individual mouse in response to decreasing value of the safe option. Every black dot represents the mean risky choices across four stable sessions with 200 trials each. Dotted lines indicate indifference point for each individual. Sigmoid fit. **b**, Cross-validated multinomial linear regression was used to predict choices using past outcomes as regressors. The performance of the model was computed from the cross-entropy loss function of predictions. Grey lines indicate performances for single mice (n=45), red thick line indicates average across mice, red thin line the standard deviation across animals. **c**, Probability of indecisive choice after sampling the non-preferred option. Mice IDs are the same as in Fig. 1c. Dots represent probability for indecisive choice after sampling the safe spout (black) or risky spout (red) in the previous trial (one black and one red probability per mouse). Model-free fit using Gaussian process regression. **d**, Fraction of engaged trials for all risk averse (cyan, n=26) and risk prone (magenta, n=15) mice. Open circles indicate fractions of engaged trials (decisive and indecisive) from all trials an animal could engaged in (300 per session in 14 sessions, 4200 trials for each mouse). **e**, Choice confidence measured as the fraction of all trials an animal could engage in subtracted by the number of indecisive trials. Results from plus maze test of animals after completion of two-alternative choice task. **f**, Fraction of time risk averse (n=20) and risk prone (n=13) mice spend in the respective part of the maze (close arm p = 0.3275; center p = 0.2445; open arm p = 0.9399; two-sided t-test). Dark circles represent data from individual mice. **g**, Number of head dips to the open arm from risk averse and risk prone animals (p = 0.151; two-sided t-test). **h**, Number of open arm entries from risk averse and risk prone animals (p = 0.1063; Mann-Whitney test).

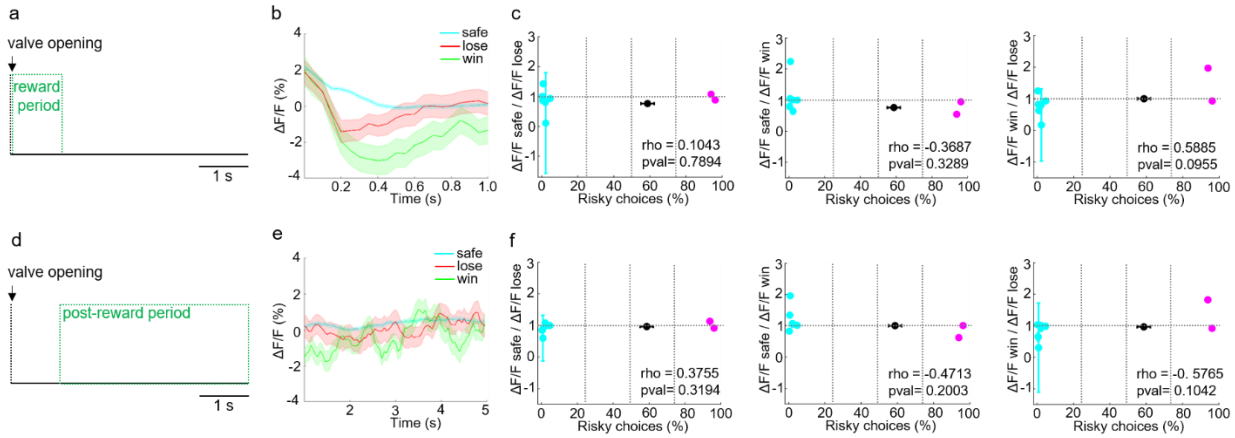

Extended Data Fig. 2 | LHb fiber photometric signal in reward and post-reward period. a, Illustration of reward period used for analysis. **b**, LHb photometry example traces from one animal aligned to reward delivery. **c**, Correlation of reward signal ratios and riskiness across animals. **d**, Illustration of post-reward period used for analysis. **e**, LHb photometry example traces for post-reward period (same animal as b). **f**, Correlation of post-reward signal ratios and riskiness across animals.

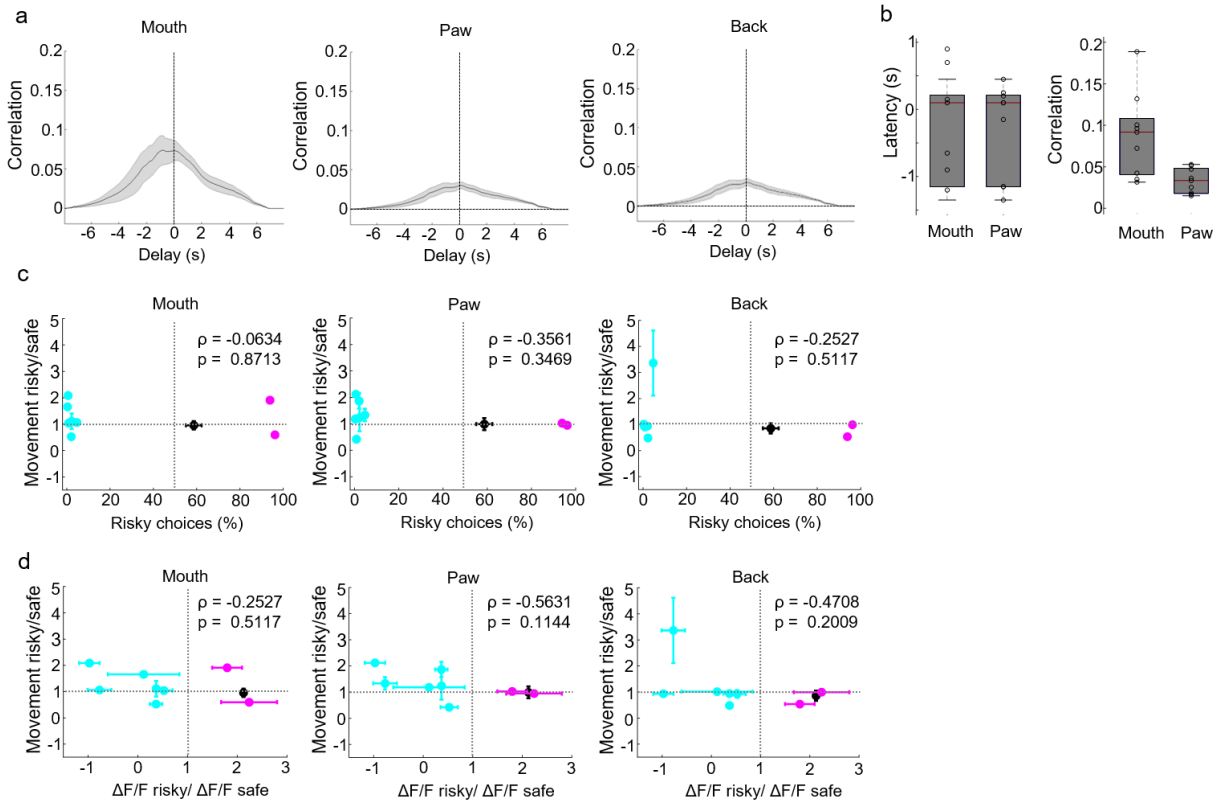

Extended Data Fig. 3 | Divergence in LHb fiber photometric signal cannot be explained by body movement. a, Cross-correlation of body movement with bulk LHb signal. Data were obtained from the same animals as in Fig. 2 d,e and are presented as mean ± s.e.m. **b**, Quantification of cross correlation latency to peak and maximum amplitude across animals. **c**, Correlation of body movement and riskiness of the respective animal. d, Correlation of body movement and LHb photometry signal in the deliberation period.

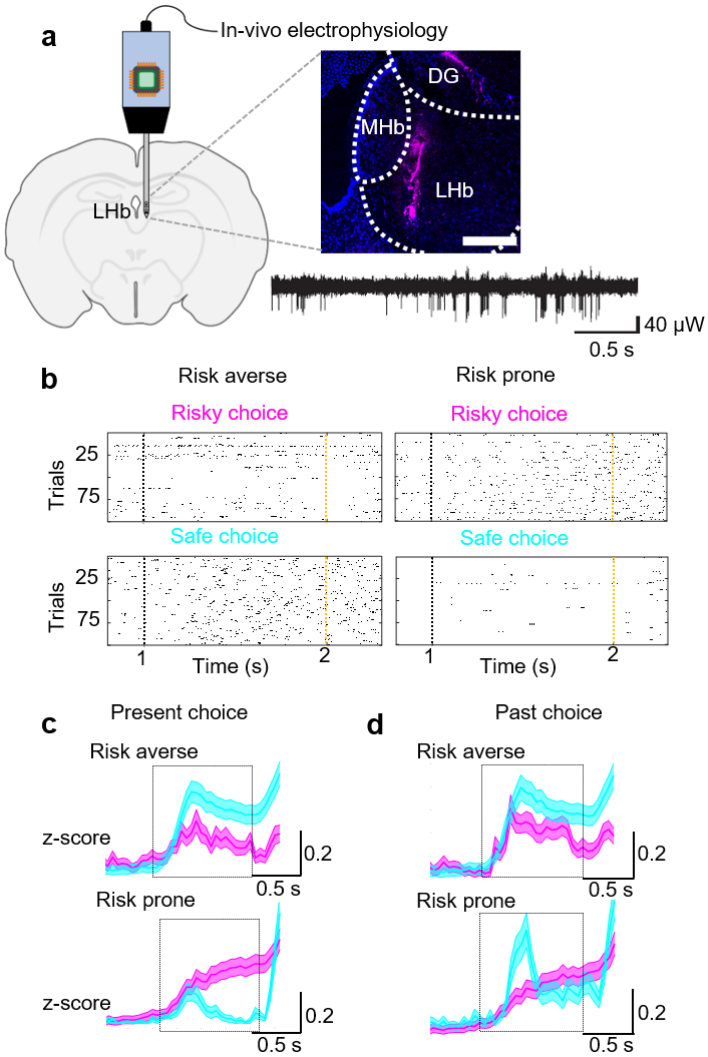

Extended Data Fig. 4 | LHb multi-unit population activity reflects risk preference. a, Illustration of silicon probe recordings with example trace. **b**, Single trial raster plots of detected action potentials. Dashed lines indicate onset of start (black) and reward (amber) cue. Merged multi-unit activity during deliberation period across all safe (cyan) and risky (magenta) trials sorted for the present (**c**) and the past choice (**d**) trial (n=4 mice). Box indicates deliberation period. Data are plotted as mean ± 95%c.i.

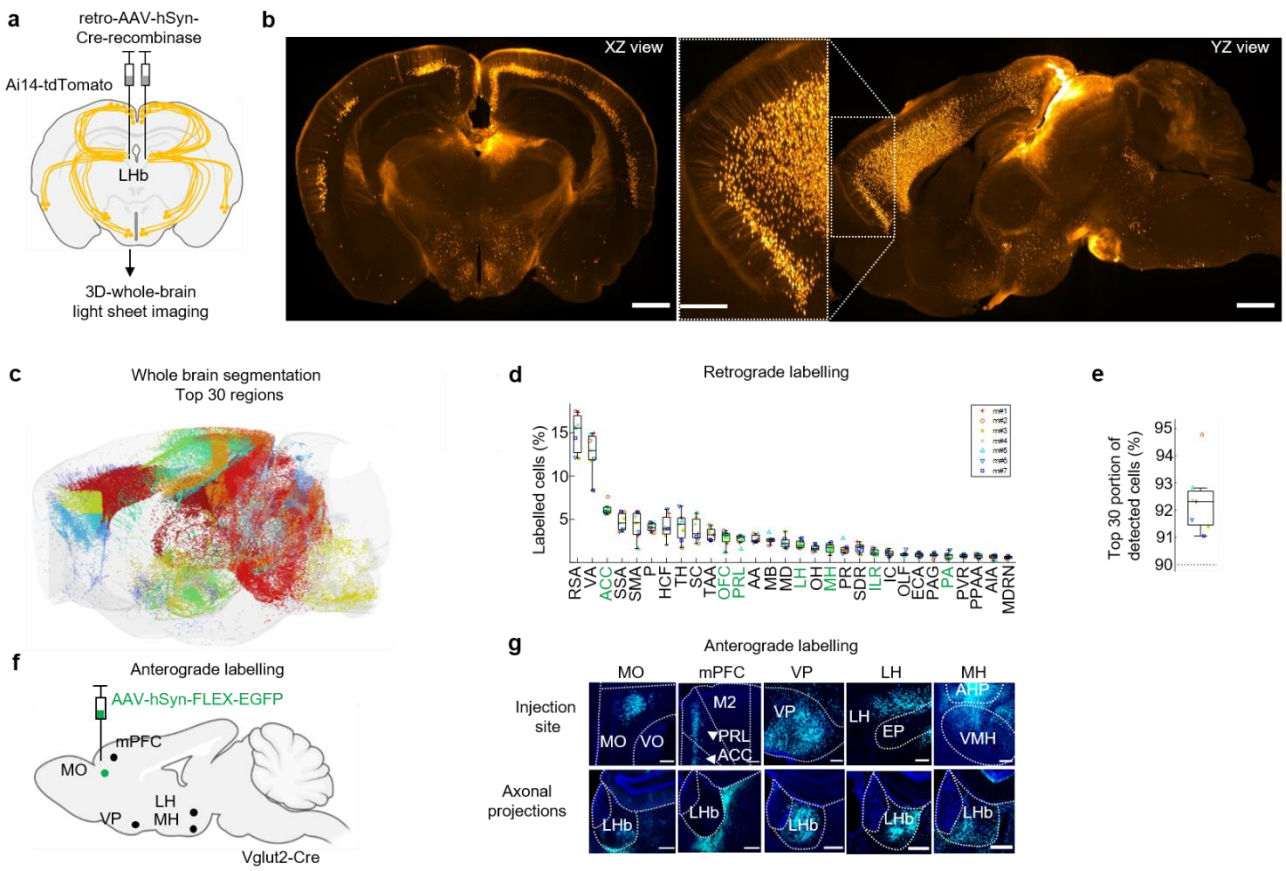

Extended Data Fig. 5 | Retrograde and anterograde AAV-labelling of LHb inputs. a, Illustration of retrograde labelling approach. Example (**b**) and segmented (**c**) image of retrogradely labelled LHb projection neurons across entire mouse brain. Neurons are coloured by brain areas; top 30 structures are shown here for the purpose of a clear visualization. Light gray outlines the brain surface. Different colours distinguish different brain regions. Scale bar represents 1 mm. **d**, Quantification of top 30 identified input regions (n=7 mice). Target areas for multi-fiber photometry highlighted in green. A detailed list of all abbreviations can be found in Supplementary Table 1. **e**, Coverage of cells detected in top 30 brain regions relative to all detected cells. **f**, Anterograde labelling of Vglut2-positive neurons and their axonal projections in the LHb from the five selected regions (medial orbital frontal cortex (MO), medial prefrontal cortex (mPFC), ventral pallidum (VP), lateral hypothalamus (LH), medial hypothalamus (MH)). Scale bars represent 200 µm.

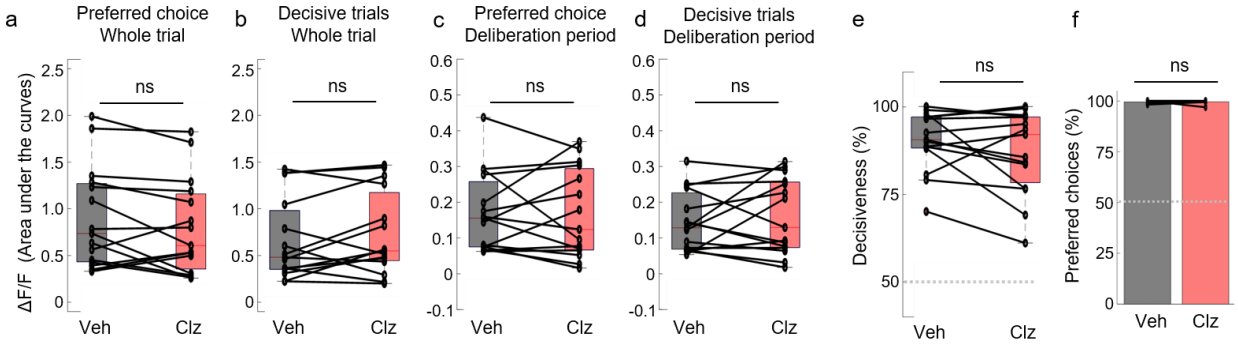

Extended Data Fig. 6 | Clozapine (0.005 mg/kg) does not impact LHb population signal and risky decision-making in mice without DREADDs. LHb fiber photometry (**a**-**d**; from respective trial types and task periods, p = 0.1688; p = 0.2293; p = 0.8904; p = 0.804; Wilcoxon-matched pairs test) and behavioural data (**e**,**f**; p = 0.1727; p = 0.7422; Wilcoxon-matched pairs test)) from vehicle and clozapine (0.005 mg/kg) sessions from mice which did not express DREADDs. Data were acquired over 15 sessions (dark circles) for each condition from three mice.

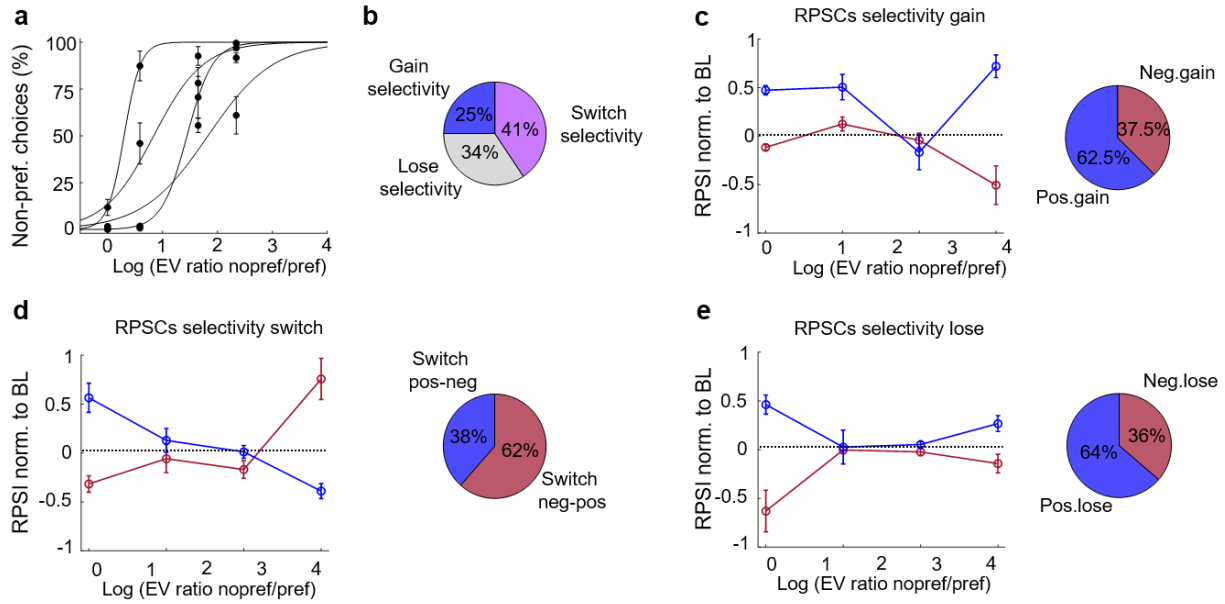

Extended Data Fig. 7 | LHb RPSCs adapt their selectivity during deliberation with changing preference. a, Fraction of non-preferred option choices with changing expected value ratio (n = 4 mice). Every dark circle represents 3-5 sessions with 200 free choice trials each. Sigmoid fit. **b**, Fractions of LHb RPSCs tracked across sessions depending on their adaptation to preference change (baseline sessions compared to last highest ratio sessions). Risk preference selectivity of negative (red) and positive (blue) LHb RPSCs depending on their responses: Cells either gain (**c**), switch (**d**), or lose (**e**) their selectivity.

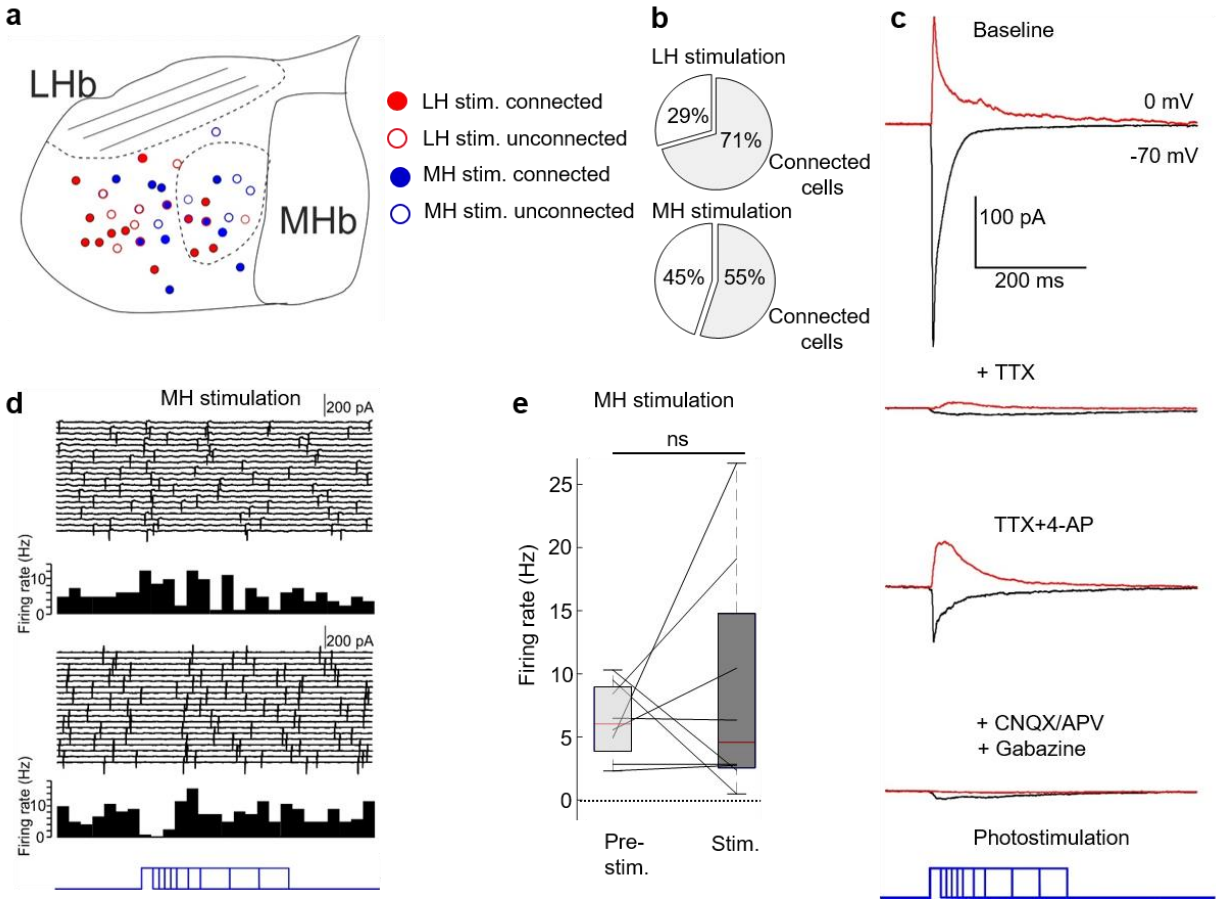

Extended Data Fig. 8 | Optogenetic stimulation of hypothalamic terminals in acute LHb containing brain slices. a, Spatial map of LHb neurons recorded in ex vivo slices. Full circles indicate connected, empty circles unconnected cells. **b**, Fraction of LHb cells showing postsynaptic responses upon optogenetic stimulation of LH (12/17 cells from 4 mice) or MH (11/20 cells from 8 mice) axons. **c**, Example traces of MH connected LHb cell show EPSCs (black) and IPSC (red) which are sensitive to sodium channel blocker tetrodotoxin (TTX). EPSCs and IPSCs are both monosynaptic connections, as they are maintained in TTX/4-AP, and sensitive to glutamate receptor antagonists (CNQX/APV), and $GABA_A$-receptor antagonist Gabazine, respectively. Example spiking traces of two MH-connected LHb neurons (**d**; band-pass filtered at 1 and 1000 Hz) and quantification (**e**) of all MH-connected LHb neurons (7 cells from 4 mice; Wilcoxon signed rank test; $p = 0.5625$) from two 20 ms bins before (pre-stim.) and during (stim.) optogenetic stimulation of MH axons.

Extended Data Table 1 | Abbreviation of retrogradely labelled LHb input regions.

Abbreviation	Brain region
RSA	Retrosplenial area
VA	Visual areas
ACC	Anterior cingulate cortex
SSA	Somatosensory areas
SMA	Somatomotor areas
P	Pons
HCF	Hippocampal formation
TH	Thalamus
SC	Superior colliculi
TAA	Temporal association areas
OA	Orbital area
PRL	Prelimbic area
AA	Auditory areas
MB	Midbrain
MD	Medulla
LH	Hypothalamic lateral zone
OH	Other hypothalamic zones
MH	Hypothalamic medial zone
PR	Pretectal region
SDR	Striatum dorsal region
ILR	Infralimbic region
IC	Inferior colliculi
OLF	Olfactory areas
ECA	Ectorhinal area
PAG	Periaqueductal grey
PA	Pallidum
PVR	Paraventricular region
PPAA	Posterior parital association areas
AIA	Agranular insular area
MDRN	Midbrain reticular nucleus

Extended Data Table 2 | Statistical tests and exact p-values.

Figure panel	Statistical test	Exact p-values
Fig. 3c	Wilcoxon rank sum test	LH: p = 0.3669; MH p = 0.0174
Fig. 3d	Wilcoxon rank sum test	LH: p = 0.4766; MH p = 0.00039
Fig. 3f	Wilcoxon rank sum test	LH: p = 0.1861; MH p = 0.00052
Fig. 3h	Wilcoxon rank sum test	LH: p = 0.00055; MH p = 0.0998
Fig. 3k	Wilcoxon signed rank test	Early (ori vs. shu) : p = 0.0049
		Late (ori vs. shu): p= 0.00049
		Early vs. shu (ori): p = 0.00049
Fig. 3l	Wilcoxon signed rank test	Early (ori vs. shu) : p = 0.6523
		Late (ori vs. shu): p= 0.0977
		Early vs. shu (ori): p = 0.0273
Fig. 3m	Wilcoxon rank sum test	LH vs. MH: p= 0.00032
Fig. 4e	Chi square test	RPSCs pos. vs. neg. : p = 0.0000006
Fig. 4g	Wilcoxon signed rank test	LH: Veh vs. Clz: p = 0.3054
		MH: Veh vs. Clz: p = 0.0137
Fig. 4h	Wilcoxon signed rank test	LH: Veh vs. Clz: p = 0.9658
		MH: Veh vs. Clz: p = 0.0195
Fig. 4i	Wilcoxon signed rank test	LH: Veh vs. Clz: p = 0.0781
		MH: Veh vs. Clz: p = 0.0093
Fig. 4 l	Wilcoxon rank sum test	LH vs. MH: p = 0.000082

References

1 Caraco, T., Martindale, S. & Whittam, T. S. An Empirical Demonstration of Risk-Sensitive Foraging Preferences. *Anim Behav* **28**, 820-830, doi:Doi 10.1016/S0003-3472(80)80142-4 (1980).

2 Tuttle, E. M., Wulfson, L. & Caraco, T. Risk-Aversion, Relative Abundance of Resources and Foraging Preference. *Behav Ecol Sociobiol* **26**, 165-171 (1990).

3 Barkan, C. P. L. A Field-Test of Risk-Sensitive Foraging in Black-Capped Chickadees (Parus-Atricapillus). *Ecology* **71**, 391-400, doi:Doi 10.2307/1940276 (1990).

4 Barnard, C. J. & Brown, C. A. J. Risk-Sensitive Foraging in Common Shrews (Sorex-Araneus L). *Behav Ecol Sociobiol* **16**, 161-164, doi:Doi 10.1007/Bf00295150 (1985).

5 Zalocusky, K. A. *et al.* Nucleus accumbens D2R cells signal prior outcomes and control risky decision-making. *Nature* **531**, 642-646, doi:10.1038/nature17400 (2016).

6 Eisenreich, B. R., Hayden, B. Y. & Zimmermann, J. Macaques are risk-averse in a freely moving foraging task. *Sci Rep* **9**, 15091, doi:10.1038/s41598-019-51442-z (2019).

7 Mata, R., Frey, R., Richter, D., Schupp, J. & Hertwig, R. Risk Preference: A View from Psychology. *Journal of Economic Perspectives* **32**, 155-172, doi:10.1257/jep.32.2.155 (2018).

8 Arslan, R. C. *et al.* How people know their risk preference. *Sci Rep* **10**, 15365, doi:10.1038/s41598-020-72077-5 (2020).

9 Stopper, C. M. & Floresco, S. B. What's better for me? Fundamental role for lateral habenula in promoting subjective decision biases. *Nat Neurosci* **17**, 33-35, doi:10.1038/nn.3587 (2014).

10 Matsumoto, M. & Hikosaka, O. Representation of negative motivational value in the primate lateral habenula. *Nat Neurosci* **12**, 77-84, doi:10.1038/nn.2233 (2009).

11 Stamatakis, A. M. & Stuber, G. D. Activation of lateral habenula inputs to the ventral midbrain promotes behavioral avoidance. *Nat Neurosci* **15**, 1105-1107, doi:10.1038/nn.3145 (2012).

12 Wang, D. *et al.* Learning shapes the aversion and reward responses of lateral habenula neurons. *Elife* **6**, doi:10.7554/eLife.23045 (2017).

13 Tritsch, N. X., Granger, A. J. & Sabatini, B. L. Mechanisms and functions of GABA co-release. *Nat Rev Neurosci* **17**, 139-145, doi:10.1038/nrn.2015.21 (2016).

14 Tobler, P. N., Fiorillo, C. D. & Schultz, W. Adaptive coding of reward value by dopamine neurons. *Science* **307**, 1642-1645, doi:10.1126/science.1105370 (2005).

15 Nakamura, K., Matsumoto, M. & Hikosaka, O. Reward-dependent modulation of neuronal activity in the primate dorsal raphe nucleus. *J Neurosci* **28**, 5331-5343, doi:10.1523/JNEUROSCI.0021-08.2008 (2008).

16 Liu, Z. *et al.* Dorsal raphe neurons signal reward through 5-HT and glutamate. *Neuron* **81**, 1360-1374, doi:10.1016/j.neuron.2014.02.010 (2014).

17 Li, Y. *et al.* Serotonin neurons in the dorsal raphe nucleus encode reward signals. *Nat Commun* **7**, 10503, doi:10.1038/ncomms10503 (2016).

18 Dabney, W. *et al.* A distributional code for value in dopamine-based reinforcement learning. *Nature* **577**, 671-675, doi:10.1038/s41586-019-1924-6 (2020).

19 Wang, R. Y. & Aghajanian, G. K. Physiological evidence for habenula as major link between forebrain and midbrain raphe. *Science* **197**, 89-91, doi:10.1126/science.194312 (1977).

20 Omelchenko, N., Bell, R. & Sesack, S. R. Lateral habenula projections to dopamine and GABA neurons in the rat ventral tegmental area. *Eur J Neurosci* **30**, 1239-1250, doi:10.1111/j.1460-9568.2009.06924.x (2009).

21 Lammel, S. *et al.* Input-specific control of reward and aversion in the ventral tegmental area. *Nature* **491**, 212-217, doi:10.1038/nature11527 (2012).

22 Zheng, Z. *et al.* Hypothalamus-habenula potentiation encodes chronic stress experience and drives depression onset. *Neuron* **110**, 1400-1415 e1406, doi:10.1016/j.neuron.2022.01.011 (2022).
23 Cerniauskas, I. *et al.* Chronic Stress Induces Activity, Synaptic, and Transcriptional Remodeling of the Lateral Habenula Associated with Deficits in Motivated Behaviors. *Neuron* **104**, 899-915 e898, doi:10.1016/j.neuron.2019.09.005 (2019).
24 Li, K. *et al.* betaCaMKII in lateral habenula mediates core symptoms of depression. *Science* **341**, 1016-1020, doi:10.1126/science.1240729 (2013).
25 Lecca, S. *et al.* Rescue of GABAB and GIRK function in the lateral habenula by protein phosphatase 2A inhibition ameliorates depression-like phenotypes in mice. *Nat Med* **22**, 254-261, doi:10.1038/nm.4037 (2016).
26 Yang, Y. *et al.* Ketamine blocks bursting in the lateral habenula to rapidly relieve depression. *Nature* **554**, 317-322, doi:10.1038/nature25509 (2018).
27 Cui, Y. *et al.* Astroglial Kir4.1 in the lateral habenula drives neuronal bursts in depression. *Nature* **554**, 323-327, doi:10.1038/nature25752 (2018).
28 Tremblay, L. & Schultz, W. Relative reward preference in primate orbitofrontal cortex. *Nature* **398**, 704-708, doi:10.1038/19525 (1999).
29 O'Neill, M. & Schultz, W. Coding of reward risk by orbitofrontal neurons is mostly distinct from coding of reward value. *Neuron* **68**, 789-800, doi:10.1016/j.neuron.2010.09.031 (2010).
30 van Holstein, M. & Floresco, S. B. Dissociable roles for the ventral and dorsal medial prefrontal cortex in cue-guided risk/reward decision making. *Neuropsychopharmacology* **45**, 683-693, doi:10.1038/s41386-019-0557-7 (2020).
31 Stephenson-Jones, M. *et al.* A basal ganglia circuit for evaluating action outcomes. *Nature* **539**, 289-293, doi:10.1038/nature19845 (2016).
32 Li, H., Pullmann, D. & Jhou, T. C. Valence-encoding in the lateral habenula arises from the entopeduncular region. *Elife* **8**, doi:10.7554/eLife.41223 (2019).
33 Stephenson-Jones, M. *et al.* Opposing Contributions of GABAergic and Glutamatergic Ventral Pallidal Neurons to Motivational Behaviors. *Neuron* **105**, 921-933 e925, doi:10.1016/j.neuron.2019.12.006 (2020).
34 Lazaridis, I. *et al.* A hypothalamus-habenula circuit controls aversion. *Mol Psychiatry* **24**, 1351-1368, doi:10.1038/s41380-019-0369-5 (2019).
35 Real, L. A. Uncertainty and Pollinator-Plant Interactions - the Foraging Behavior of Bees and Wasps on Artificial Flowers. *Ecology* **62**, 20-26, doi:Doi 10.2307/1936663 (1981).
36 Matsumoto, M. & Hikosaka, O. Lateral habenula as a source of negative reward signals in dopamine neurons. *Nature* **447**, 1111-1115, doi:10.1038/nature05860 (2007).
37 Hong, S., Jhou, T. C., Smith, M., Saleem, K. S. & Hikosaka, O. Negative reward signals from the lateral habenula to dopamine neurons are mediated by rostromedial tegmental nucleus in primates. *J Neurosci* **31**, 11457-11471, doi:10.1523/JNEUROSCI.1384-11.2011 (2011).
38 Shabel, S. J., Wang, C., Monk, B., Aronson, S. & Malinow, R. Stress transforms lateral habenula reward responses into punishment signals. *Proc Natl Acad Sci U S A* **116**, 12488-12493, doi:10.1073/pnas.1903334116 (2019).
39 Lalive, A. L. *et al.* Synaptic inhibition in the lateral habenula shapes reward anticipation. *Curr Biol*, doi:10.1016/j.cub.2022.02.035 (2022).
40 Trusel, M. *et al.* Punishment-Predictive Cues Guide Avoidance through Potentiation of Hypothalamus-to-Habenula Synapses. *Neuron* **102**, 120-127 e124, doi:10.1016/j.neuron.2019.01.025 (2019).

41 Yetnikoff, L., Cheng, A. Y., Lavezzi, H. N., Parsley, K. P. & Zahm, D. S. Sources of input to the rostromedial tegmental nucleus, ventral tegmental area, and lateral habenula compared: A study in rat. *J Comp Neurol* **523**, 2426-2456, doi:10.1002/cne.23797 (2015).
42 Bernard, R. & Veh, R. W. Individual neurons in the rat lateral habenular complex project mostly to the dopaminergic ventral tegmental area or to the serotonergic raphe nuclei. *J Comp Neurol* **520**, 2545-2558, doi:10.1002/cne.23080 (2012).
43 Quina, L. A. *et al.* Efferent pathways of the mouse lateral habenula. *J Comp Neurol* **523**, 32-60, doi:10.1002/cne.23662 (2015).
44 Gilad, A., Gallero-Salas, Y., Groos, D. & Helmchen, F. Behavioral Strategy Determines Frontal or Posterior Location of Short-Term Memory in Neocortex. *Neuron* **99**, 814-828 e817, doi:10.1016/j.neuron.2018.07.029 (2018).
45 Owen, S. F., Liu, M. H. & Kreitzer, A. C. Thermal constraints on in vivo optogenetic manipulations. *Nat Neurosci* **22**, 1061-1065, doi:10.1038/s41593-019-0422-3 (2019).
46 Chuong, A. S. *et al.* Noninvasive optical inhibition with a red-shifted microbial rhodopsin. *Nat Neurosci* **17**, 1123-1129, doi:10.1038/nn.3752 (2014).
47 Gomez, J. L. *et al.* Chemogenetics revealed: DREADD occupancy and activation via converted clozapine. *Science* **357**, 503-507, doi:10.1126/science.aan2475 (2017).
48 Zerbi, V. *et al.* Rapid Reconfiguration of the Functional Connectome after Chemogenetic Locus Coeruleus Activation. *Neuron* **103**, 702-718 e705, doi:10.1016/j.neuron.2019.05.034 (2019).
49 Pachitariu, M. *et al.* Suite2p: beyond 10,000 neurons with standard two-photon microscopy. *bioRxiv*, 061507, doi:10.1101/061507 (2017).
50 Rupprecht, P. & Friedrich, R. W. Precise Synaptic Balance in the Zebrafish Homolog of Olfactory Cortex. *Neuron* **100**, 669-683 e665, doi:10.1016/j.neuron.2018.09.013 (2018).
51 Junek, S., Chen, T. W., Alevra, M. & Schild, D. Activity correlation imaging: visualizing function and structure of neuronal populations. *Biophys J* **96**, 3801-3809, doi:10.1016/j.bpj.2008.12.3962 (2009).
52 Renier, N. *et al.* iDISCO: a simple, rapid method to immunolabel large tissue samples for volume imaging. *Cell* **159**, 896-910, doi:10.1016/j.cell.2014.10.010 (2014).
53 Voigt, F. F. *et al.* The mesoSPIM initiative: open-source light-sheet microscopes for imaging cleared tissue. *Nat Methods* **16**, 1105-1108, doi:10.1038/s41592-019-0554-0 (2019).
54 Kirst, C. *et al.* Mapping the Fine-Scale Organization and Plasticity of the Brain Vasculature. *Cell* **180**, 780-795 e725, doi:10.1016/j.cell.2020.01.028 (2020).